Geochimica et Cosmochimica Acta 394 (2025) 106–125

Contents lists available at ScienceDirect

Geochimica et Cosmochimica Acta

journal homepage: www.elsevier.com/locate/gca

Ultra-fast metamorphic reaction during regional metamorphism

Jia-Hui Liu [a,b,c,*], Pierre Lanari [b,d], Renée Tamblyn [b], Hugo Dominguez [b], Jörg Hermann [b], Daniela Rubatto [b,d], Jacob B. Forshaw [b], Francesca Piccoli [b], Qian W.L. Zhang [a,b,c], Thorsten A. Markmann [b], Julien Reynes [b,d], Zhen M.G. Li [c], Shujuan Jiao [a,c], Jinghui Guo [a,c]

[a] *State Key Laboratory of Lithospheric and Environmental Coevolution, Institute of Geology and Geophysics, Chinese Academy of Sciences, Beijing 100029, China*
[b] *Institute of Geological Sciences, University of Bern, Bern 3012, Switzerland*
[c] *College of Earth and Planetary Sciences, University of Chinese Academy of Sciences, Beijing, 100049, China*
[d] *Institute of Earth Sciences, University of Lausanne, Géopolis 1015 Lausanne, Switzerland*

ARTICLE INFO

Associate Editor: Olivier Namur

Keywords:
Timescales
Metamorphic reaction
Mineral growth
Diffusion chronometry
Trace elements

ABSTRACT

Constraining the timescales of metamorphic processes is critical to understanding geodynamics on Earth. It is generally accepted that the rates of metamorphic reactions in regional metamorphism, where fluids are limited or transient, are several orders of magnitude slower than in laboratory experiments. This discrepancy is attributed to several rate-limiting mechanisms affecting metamorphic reactions in natural settings, such as differences in the reactive surface area of the reactants, the magnitude of the driving force for reaction, rates of inter-granular transport and possible fluid content. Here we report an ultra-fast metamorphic reaction within a year, constrained by diffusion modeling on frozen-in chemical gradients of trace elements preserved in metamorphic garnet across a partially melted corona texture. The growth of peritectic garnet occurred in the presence of a melt phase, which distributed along the grain boundaries. The observed chemical gradient of HREE+Y in garnets is interpreted to have formed due to trace element diffusion in the inter-granular melt, recorded by the simultaneous growth of multiple garnet grains across the corona texture. A diffusion model using a fixed boundary condition suggests a timescale of 8.4 (+5.4/-3.3) days for the formation of this corona texture, whereas a moving boundary model provides a slightly longer timescale of less than a year. These timescales are much shorter than those previously obtained from regional metamorphism in nature, but are similar to contact metamorphism in nature and laboratory-based results. Based on these findings, we propose that ultra-fast pulses of metamorphic reactions occur in nature under fluid/melt-present conditions, as elemental diffusion and mass transport in an aqueous fluid or melt are significantly faster than those in mineral lattices and anhydrous grain boundaries. However, rapid metamorphic reactions are difficult to identify due to the insufficient temporal resolution of radioisotope dating and the poor preservation of chemical gradients during subsequent metamorphic reactions.

1. Introduction

The dissolution and growth of minerals during metamorphism, along with the associated changes in their physical properties, control key processes in the solid Earth, such as mineralization and seismic events (Incel et al., 2017; Obara, 2002; Pitcairn et al., 2021; Wang et al., 2004; Malvoisin et al., 2020). These processes also underpin our understanding of reaction kinetics, fluid-rock interaction processes, elemental transport and partitioning in geodynamic systems, such as collisional orogens and subduction zones. While the pressure–temperature–composition (*P*–*T*–*X*) conditions driving these changes are well known, the rates or timescales of metamorphic reactions remain a topic of ongoing debate (Baxter, 2003; Baxter and DePaolo, 2000; Chakraborty et al., 2016; Cruz-Uribe et al., 2014; Negi et al., 2014; Rubie and Thompson, 1985; Rubie, 1986, 1998). Based on case studies on metamorphic reaction rates from measurements on natural samples and a review of previous works, Baxter (2003) and Baxter and DePaolo (2000) proposed the paradigm that metamorphic reaction rates of lab-based experiments are four to seven orders of magnitude faster than those measured in natural systems. The rates of

---

* Corresponding author at: State Key Laboratory of Lithospheric and Environmental Coevolution, Institute of Geology and Geophysics, Chinese Academy of Sciences, Beijing 100029, China.

E-mail address: liujiahui@mail.iggcas.ac.cn (J.-H. Liu).

https://doi.org/10.1016/j.gca.2025.01.036
Received 20 September 2024; Accepted 24 January 2025

metamorphic reactions were calculated or defined by reacted quantity (mineral dissolution or growth, material exchange; in moles, grams, or gram-atoms oxygen) per surface area of the rate-limiting mineral per time. They attributed the discrepancy to rate-limiting mechanisms between natural and experimental systems, such as differences in the reactive surface area of the reactants, the magnitude of the driving force for reaction, rates of inter-granular transport and possible transient spurts of fluid content. Rubie and Thompson (1985) and King et al. (2010) highlighted that rates observed in experimental systems cannot easily be extrapolated to natural systems, due to differences in mineral powder properties, stress, and compaction lengths. Contrary to these findings, studies based on rate-calculation methods have suggested that fluid infiltration can trigger rapid metamorphic reactions over days to ten thousand years (Rubie, 1986, 1998; Walther and Wood, 1984).

These points of view are not irreconcilable. Many reaction rates are estimated by calculating the durations of metamorphic reactions and converting them into reaction rates, thus representing average reaction rates (Baxter, 2003; Baxter and DePaolo, 2000; Cruz-Uribe et al., 2014). Natural mineral reactions during regional metamorphism are complex and may occur as reaction pulses in response to fluid influx or other external effects (Cruz-Uribe et al., 2014; Dragovic et al., 2015; Tual et al., 2022). For example, it has been suggested that rapid metamorphic reactions induced by seismicity or overpressure can occur within a thousand years (Camacho et al., 2005; Chu et al., 2017). However, a key open question remains: do fast metamorphic pulses, comparable to those observed in the laboratory experiments, also occur during common regional metamorphism?

Garnet provides valuable insights into the timescales and conditions of metamorphic events due to its growth across a broad *P*–*T* range. It frequently preserves major and trace element zoning, which records growth conditions and/or diffusional processes and can be dated by various geochronometers. The fastest growth duration of metamorphic garnet during regional metamorphism obtained by Sm-Nd situ-dating is 0.04–0.7 Myr (Pollington & Baxter, 2010) and by Lu-Hf situ-dating is 0.1–0.2 Myr (Tual et al., 2022). However, this temporal resolution of tens to hundreds of thousands of years cannot resolve shorter-lived pulses of mineral growth. Diffusion chronometry is a high-temporal resolution technique used to infer timescales from the inversion of chemical diffusion profiles in phases, which offers great potential to probe short durations on the order of days to hundreds of years (e.g., Antonelli et al., 2019; Caracciolo et al., 2021; Costa et al., 2003; Viete and Lister, 2017). Currently, diffusion chronometry in metamorphic studies is primarily applied to intra-crystal diffusion modeling to constrain the near-peak/cooling timescale after mineral growth (e.g., Ague and Baxter, 2007; Jollands et al., 2018; Rubatto et al., 2020; Viete and Lister, 2017; Walther and Wood, 1984). More rarely, it is used to constrain the timescale of metamorphic reactions involving both the dissolution and growth of metamorphic minerals (e.g., Chu et al., 2018). The metamorphic reactions are considered to include two rate-limiting end-member processes: (a) interface-controlled, i.e., dissolution and growth of minerals, and the release and incorporation of element/material during this process; (b) diffusion-controlled, i.e., transport and diffusion of element/material through inter-crystal medium between reaction sites (Carlson, 1989, 1991, 2011; Daniel and Spear, 1998; Fisher, 1978; Kretz, 1973; Spear and Daniel, 1998; Spear and Daniel, 2001). Metamorphic reactions can occur no faster than is permitted by the slowest mechanism, the rate-limiting process (Fisher, 1978). A diffusion-controlled metamorphic reaction may record the diffusion of elements in the inter-crystalline medium and allow the timescale of mineral reactions to be constrained.

Coronal reaction textures in metamorphic rocks are generally considered as disequilibrium textures and may record information about disequilibrium growth of a mineral, especially if their chemical composition is controlled by diffusion driven by chemical potential gradients (Ashworth and Sheplev, 1997; Du et al., 2023; Gaidies et al., 2017; Ghosh et al., 2021; Grant, 1988; Johnson and Carlson, 1990; Larikova and Zaraisky, 2009; White et al., 2008). Therefore, these textures have the potential to preserve information about inter-granular diffusion, and could serve to study metamorphic reaction rates using diffusion chronometry.

In this contribution, we investigated two nearby metagabbros (metagabbro A & B) from the Trans-North China Orogen (TNCO), which exhibit granoblastic and coronal reaction textures, respectively, at the peak stage of the granulite-facies metamorphism (see section 4.1). Petrography, geothermobarometry, geochronology, and water budget calculation studies were carried out to unravel both the magmatic and metamorphic history of these two metagabbro samples. On this basis, we applied a novel multi-phase trace element mapping technique (Markmann et al., 2024) to image the trace element gradient across several garnet grains of the corona, and determine whether it records the elemental diffusion in the inter-granular medium. Finally, additional mass balance calculations, and diffusion modeling were performed to examine the reaction mechanism and to constrain the metamorphic reaction/mineral growth timescales.

2. Geological setting

Metagabbro samples A and B were collected from the Fuping Terrane, TNCO, North China Craton (NCC) (Fig. 1 & Fig. S1). The NCC is composed of Early Archean to Paleoproterozoic basement covered by Mesoproterozoic to Cenozoic sediment (Zhao et al., 2005). The basement of the NCC was formed via collision and amalgamation of the Eastern and Western Blocks along the TNCO during the Late Paleoproterozoic. The Fuping Terrane lies in the middle TNCO, and comprises tonalite-trondhjemite-granodiorite (TTG) gneiss containing mafic granulite enclaves recording regional metamorphism with peak conditions of 800–900 °C / 0.7–1.4 GPa at 1.92–1.80 Ga (Liu et al., 2021; Zhao et al., 2000). The studied gabbro protoliths were emplaced within the TTG gneiss thirty meters apart from each other (Fig. 1). The GPS locations are 114°11′36″ E, 38°48′41″ N for metagabbro A, and 114°11′36″ E, 38°48′39″ N for metagabbro B.

3. Methods

3.1. Data collection

Details of the methods used for mineral major and minor element chemical compositional analyses, trace element single-spot analyses of clinopyroxene, bulk-rock chemical compositional analyses, zircon U–Pb geochronological analyses, and mineral water content analyses are provided in the supplementary methods.

Trace element single-spot analyses of minerals other than clinopyroxene and maps of minerals were conducted on a Laser Ablation Inductively Coupled Plasma Mass Spectrometry (LA-ICP-MS) using a Resonetics RESOlutionSE 193 nm excimer laser system equipped with an S-155 large-volume constant-geometry chamber at the Institute of Geological Sciences, University of Bern, Switzerland. The laser system was coupled to an Agilent 7900 quadrupole ICP-MS instrument. NIST612 (Pearce et al., 1997) and GSD-1G (Jochum et al., 2005) were used as reference materials. The single-spot analytical conditions were a repetition rate of 5 Hz, laser fluence of 4~6 J/cm^2, and circular ablation spot size of 16~64 μm in diameter. The spot-analysis data were reduced with the software Iolite (Hellstrom et al., 2008; Paton et al., 2011). The maps were performed with a repetition rate of 10 Hz, laser fluence of 7 J/cm^2, circular ablation spot size of 20 μm in diameter, and a scan rate of 120 μm/s. The laser maps were classified and calibrated using XMapTools 4.1 (Lanari et al., 2019; Lanari et al., 2014; Lanari and Piccoli, 2020; Lanari et al., 2023; Markmann et al., 2024).

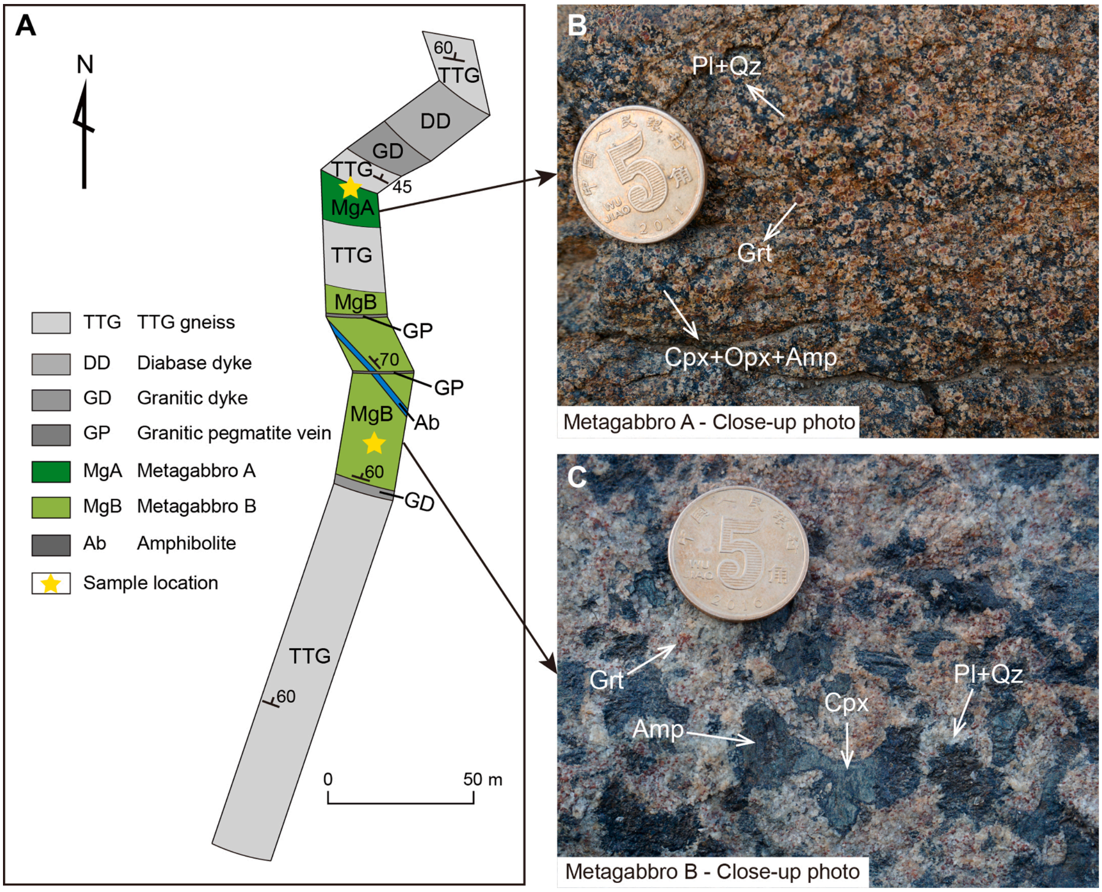

Fig. 1. Sketch and close-up photos of metagabbro A and B. (A) Geological map of a transect across metagabbro A and metagabbro B. (B–C) Close-up photos of metagabbro A and B.

3.2. *Quantitative calculations*

3.2.1. *Phase equilibrium modeling*

Phase equilibrium modeling was used to estimate metamorphic *P*–*T* conditions for metagabbro A and B. Metagabbro samples were modeled in the system $MnO–Na_2O–CaO–K_2O–FeO–MgO–Al_2O_3–SiO_2–H_2O–TiO_2–O$ (Fe_2O_3) using Perple_X (ver. 6.9.0; Connolly, 2005) with the thermodynamic dataset of Holland and Powell (2011). Quartz, titanite and rutile are considered as pure phases, the fluid phase is assumed to be pure H_2O. The phases considered in the modeling and the corresponding activity-composition solution models are: garnet, orthopyroxene, muscovite, biotite (White et al., 2014a; White et al., 2014b); clinopyroxene, amphibole and melt (Green et al., 2016); plagioclase and K-feldspar (Holland and Powell, 2003); epidote (Holland and Powell, 2011); ilmenite (White et al., 2000); spinel (White et al., 2002). Water content in the model was estimated using temperature–water content (T–M_{H2O}) diagrams with H_2O contents ranging from near-anhydrous to a more hydrous composition. Suitable water contents were selected at the conditions where the peak mineral assemblage was predicted to be stable, and then were fixed in the *P*–*T* diagrams. The estimated uncertainties of phase equilibrium modeling are ± 50 °C and at least ± 0.10 GPa (2σ, Powell and Holland, 2008).

3.2.2. *Water budget calculation*

The water budget for metagabbro B was estimated to assess the amount of water that was added to the rock during metamorphism, and to further understand its effect on the formation of the different textures observed (see section 4.2.2). Metagabbro B contains mineral relics from both igneous and metamorphic stages and shows no retrogression. The difference in water content between igneous and metamorphic stages is taken to represent the water budget that was added to the rock during metamorphism. The calculation was not applied to metagabbro A, which has undergone more complex processes, including post-peak retrogression at multiple stages. Instead, the water content estimated from T–M_{H2O} phase diagrams that stabilizes the peak mineral assemblage was used to constrain the water budget for metagabbro A.

The aqueous fluid phase is considered to be pure H_2O and the system is open to fluid infiltration during metamorphism, i.e. the system can be hydrated between the igneous and metamorphic stages. For the igneous stage, the volume of each original igneous mineral is represented by the sum of its igneous relics and the metamorphic minerals that formed from it based on the reaction texture. The metamorphic stage includes metastable igneous relics and metamorphic minerals, and the volume of each mineral phase can be directly observed. The mineral volumes are approximately estimated by the mineral surface area (automatically calculating the pixel numbers in each phase) obtained using XMapTools (Lanari and Engi, 2017). Volume fractions were converted to weight fractions using:

$$w_i = \frac{\rho_i}{\rho_{\text{average}}} v_i \tag{1}$$

where ρ_i is the density of the phase i, ρ_{average} is the average density of the area, v_i is the volume fraction of the phase i, and w_i is the weight fraction of the phase i (Lanari and Engi, 2017). The water budget for both igneous and metamorphic stages was obtained using:

$$W_{\text{total}}^{\text{H2O}} = \sum_{i=1}^{n} w_i W_i^{\text{H2O}} \tag{2}$$

where $W_{\text{total}}^{\text{H2O}}$ is the water weight fraction in each stage (water budget); W_i^{H2O} is the water weight fraction in phase i, which was estimated by stoichiometry from EPMA analyses for hydrous phases, and by FTIR analyses for nominally anhydrous phases (see supplementary method).

3.2.3. Mass balance calculation for HREE+Y

Mass balance of HREE+Y contents were calculated for the igneous and metamorphic stages in metagabbro B. The approach to reconstruct the volume of igneous and metamorphic minerals is given in section 3.2.2. Assuming a closed system behavior for HREE+Y, the total HREE+Y content measured in the bulk rock was used as the total budget for both the igneous and the metamorphic stages. For the igneous stage, the HREE+Y in igneous minerals (unknown compositions) was estimated from the mass balance equation:

$$W_{\text{total}}^{\text{HREE+Y}} = \sum_{i=1}^{n} w_i W_i^{\text{HREE+Y}} \tag{3}$$

where $W_{\text{total}}^{\text{HREE+Y}}$ is HREE+Y weight fraction in the bulk rock, $W_i^{\text{HREE+Y}}$ is the HREE+Y weight fraction in phase *i*. The amount of HREE+Y in igneous minerals (known compositions) was obtained from LA-ICP-MS analyses of unmodified crystals and assumed to satisfy Eq. (3).

During the metamorphic stage, the total HREE+Y content in igneous relics was obtained using Eq. (3); the total HREE+Y content in metamorphic minerals was obtained from the difference between bulk rock composition and the total amount of HREE+Y preserved in the igneous relics:

$$W_{\text{MM}}^{\text{HREE+Y}} = W_{\text{bulk}}^{\text{HREE+Y}} - W_{\text{IR}}^{\text{HREE+Y}} \tag{4}$$

where $W_{\text{MM}}^{\text{HREE+Y}}$ is HREE+Y weight fraction in metamorphic minerals, $W_{\text{bulk}}^{\text{HREE+Y}}$ is HREE+Y weight fraction in bulk rocks, $W_{\text{IR}}^{\text{HREE+Y}}$ is HREE+Y weight fraction in igneous relics. HREE+Y partitioning in each metamorphic mineral and a possible melt phase was computed based on the partitioning coefficient (K_{d}) of HREE+Y between mineral and melt in granulite facies (e.g, Nehring et al., 2009) using:

$$W_i^{\text{HREE+Y}} = \frac{{K_{\text{d}}}_i^{\text{HREE+Y}}}{{K_{\text{d}}}_{\text{average}}^{\text{HREE+Y}}} W_{\text{MM}}^{\text{HREE+Y}} \tag{5}$$

where ${K_{\text{d}}}_i^{\text{HREE+Y}}$ is the HREE+Y K_{d} between each phase *i* and remaining melt (which is equilibrated with metamorphic minerals), ${K_{\text{d}}}_{\text{average}}^{\text{HREE+Y}}$ is the average K_{d} for the whole metamorphic minerals of metamorphic stage. Finally, the HREE+Y weight fraction in the initial melt (before crystallization of all metamorphic minerals and their absorption of HREE+Y from it) was calculated using Eq. (3).

3.3. Diffusion modeling

3.3.1. HREE+Y diffusion modeling in melt using a fixed boundary model

The diffusion of HREE+Y was treated as single-component diffusion of elements present in trace amounts in a homogeneous melt medium along a one-dimensional semi-infinite profile. The diffusion was assumed to be dictated by the Fick's second law of diffusion (Crank, 1975):

$$\frac{\partial C}{\partial t} = D\frac{\partial^2 C}{\partial x^2} \tag{6}$$

Here, the composition *C* is expressed in μg/g; the density of the melt is assumed to be constant throughout the profile. The diffusion coefficient *D* (in m^2/s) is temperature *T* dependent and defined as the following Arrhenius equation and finally transformed as $\mu\text{m}^2/\text{day}$ for convenience:

$$D = D_0 \exp\left(\frac{-E_{\text{a}}}{\text{R}T}\right) \tag{7}$$

where D_0 is the pre-exponential factor in m^2/s, E_{a} is the activation energy for diffusion in J/mol, R is the gas constant in J/(K·mol) and *T* is temperature in Kelvin.

Diffusion of HREE+Y in melt was modeled to reproduce HREE+Y gradients preserved between several garnet grains in metagabbro B. This is based on the assumption that HREE+Y gradients were formed by diffusion in the inter-granular melt and captured/inherited by nearby garnet growth. Mass balance calculation demonstrates that HREE+Y gradients in garnets can be used as proxy of HREE+Y in the melt (see section 4.4). Representative HREE+Y compositional profiles in garnet were extracted using the tool "Sampling-Strip" implemented in XMapTools. The compositional profiles were located perpendicular to the corona texture and across several garnet grains from proximal to igneous clinopyroxene relics (P2Cpx_{I}) to proximal to igneous plagioclase relics (P2Pl_{I}). Six compositional profiles were extracted along six transects (Tr), including four unilateral diffusion profiles (Tr1–Tr4, diffusion from igneous clinopyroxene on one side and to igneous plagioclase on the other side) and two bilateral diffusion profiles (Tr5–Tr6, diffusion from igneous clinopyroxene at both ends and to the igneous plagioclase in the middle). A few pixel analyses located at mineral boundaries do not conform with the overall trend of compositional profiles; these are interpreted to result from the mixing of compositions from two minerals and were removed.

The initial profile for diffusion was generated for each element in each profile using a step function ($t = 0$), assuming that the compositions in the melt were flat on the side of igneous plagioclase. The center position was fixed on the second analysis for unilateral profiles, and was fixed on the second and second to last analyses for the bilateral profiles. The maximum value of the step function was selected from the maximum value in the measured profiles, while the flat values were selected from the average of several minimum values in the measured profiles.

A diffusion program was developed in MATLAB© for multi-element and multi-profile diffusion modeling with uncertainty propagation. Experimental diffusion coefficients (D_{exp}) and related uncertainties were obtained for all elements, by employing the Monte Carlo method using 5000 repetitions simulating the uncertainty variations of all model parameters [± 25 °C of *T* (at 1σ) and D_0 and E_{a} uncertainties from Holycross and Watson (2018)]. D_0 and E_{a} uncertainties were propagated using a correlation coefficient of 0.95 as they follow the compensation law (e.g., Holycross and Watson, 2016). The observed compositional profiles represent diffusion at time *t*, whereas the step function profiles represent diffusion at time 0.

The diffusion modeling was carried out to estimate a diffusion time for multi-elements and multi-profiles together. Assuming a starting value of *t*, a global diffusion of all elements from all profiles was modeled by solving Eq. (6). This was done by discretizing in space using centred finite differences and by integrating in time with the implicit Euler method. The value of *t* was obtained by Nelder-Mead non-linear optimization as the value minimizing the sum of residuals ($\mathit{Residual}_{\text{total}}$) between the modeled and observed profiles for all elements of all profiles. The inversion allows a value of *t* (5000 results) to be determined for all elements and all profiles considered together.

3.3.2. HREE+Y diffusion modeling in melt using a moving boundary model

One of the assumptions of the numerical approach in section 3.3.1 is to consider a constant infinite reservoir on the side of igneous clinopyroxene of the model providing the supply of trace elements. This is formulated by applying a Dirichlet boundary condition. To be able to assess how the availability of trace elements at the clinopyroxene-melt interface impact the prediction of the melt composition, a different approach involving a Neumann boundary condition is required. Using the clinopyroxene-melt interface as a moving reference frame, a moving boundary model using a 1D advection–diffusion formulation can be expressed with the following equation:

$$\frac{\partial C}{\partial t} = D\frac{\partial^2 C}{\partial x^2} - r\frac{\partial C}{\partial x} \tag{8}$$

with r, the growth rate of crystal (μm/s), here negative representing dissolution rate of igneous clinopyroxene. Lu was selected as an example of HREE+Y. Compared to Eq. (6), an advection term is added to move the reference frame following the clinopyroxene-melt interface through the model. The boundary conditions become:

$$\left.\frac{\partial C}{\partial x}\right|_{x=0} = \frac{-r}{D}\left(\frac{1}{K_{\text{melt/Cpx}}} - 1\right)C \tag{9a}$$

$$C|_{x=\infty} = 0 \tag{9b}$$

with $K_{\text{melt/Cpx}}$ the constant coefficient between the Lu in melt and in igneous clinopyroxene (see section 4.4). Eq. (9a) is a Neumann boundary condition derived from the mass balance between the chemical flux produced by the clinopyroxene consumption and the chemical flux transported away from the interface by diffusion. This is based on the assumption that the reaction kinetics of clinopyroxene consumption is fast with respect to the diffusion timescale (e.g., Glicksman, 2011; Phelps et al., 2020). The boundary condition of Eq. (9b) assumes that the melt composition remains constant at distances greater than the diffusive length scale.

Eqs. (8), (9a) and (9b) were solved numerically. For the initial conditions, the mass fraction of Lu in the melt is defined as 0 μg/g on all the model. The total size of the domain is 10,000 μm to simulate a semi-infinite profile and prevent boundary effects, but only the first 3,000 μm are presented on the numerical results. The equations were discretized in space using finite differences on a regular grid composed of 3,000 grid points and integrated in time implicitly using the trapezoidal rule with the second order backward difference formula (Bank et al., 1985). This was done with the Julia programming language using the package DifferentialEquations.jl (Bezanson et al., 2017; Rackauckas and Nie, 2017). The solver uses adaptive time-stepping and the Newton method as a non-linear solver, using forward automatic differentiation to compute the Jacobian matrix (Revels et al., 2016).

It is assumed that the product of clinopyroxene consumption is amphibole and melt, and the HREE+Y in the melt is absorbed by amphibole as it passes through the domain with the crystallizing amphibole. Then the Lu diffusion profile in the remaining melt can almost represent the diffusion profile just before absorption by garnet grains. The mass balance and partitioning calculation in this part follow the method in section 3.2.3. The average values of Lu mass fraction in igneous clinopyroxene and metamorphic amphibole, and the volume fraction of metamorphic amphibole and melt were used for calculation. $K_{\text{melt/Cpx}}$ is calculated to be a constant coefficient between the initial value in melt and the average value in igneous clinopyroxene and was used in the model according to Eq. (9a).

4. Results

4.1. Petrography and geochemistry

The bulk-rock compositions of metagabbro A and B are almost identical in major and trace elements (Fig. S2; Table S1), indicating these two metagabbros may share the same igneous protolith. The sampled metagabbros A and B display different textures. Metagabbro A exhibits an equilibrated granoblastic texture at granulite facies conditions that is overprinted by a corona texture developed during retrograde metamorphism. Metagabbro B shows a disequilibrium corona texture of granulite facies minerals overgrowing igneous relics. This sample was investigated in detail by petrography and geochemical analyses, mass balance calculation and diffusion modeling. Metagabbro A is only used for comparison and was studied in less detail.

4.1.1. Metagabbro A

Metagabbro A shows a granoblastic texture consisting of amphibole (~28 vol%), plagioclase (~25%, mainly andesine and minor albite), garnet (~15%), clinopyroxene (~13%), quartz (~10%), orthopyroxene (~7%), and accessory minerals (~2%) including ilmenite, apatite, and zircon (Fig. 1B and Fig. 2A). The mineral proportions were estimated through micropetrography observations. Two main stages of mineral equilibration [p-peak, r-retrograde; mineral abbreviations follow Warr (2021)] are recognized based on the mineral chemical compositions (Fig. S3A–D; Table S2) and reaction textures. Garnet shows an initial decrease in X_{Sps} [= Mn/(Fe^{2+}+Mg+Ca+Mn)] and increase in X_{Mg} [= Mg/(Mg+Fe^{2+})] from core to inner rim, as typical of garnet growth during prograde metamorphism (Hollister, 1966; Spear et al., 1990); the subsequent increase in X_{Sps} and decrease in X_{Mg} in the outermost rim imply consumption of garnet during retrogression (Kohn and Spear, 2000). Therefore, the compositions of the garnet inner rim most likely represent the peak stage. In general, the peak minerals mainly include the granoblastic minerals: garnet inner rim (Grt_{p}), clinopyroxene (Cpx_{p}), ± orthopyroxene (Opx_{p}), amphibole (Amp_{p}), plagioclase (Pl_{p}), and quartz (Qz_{p}). The retrograde stage is represented by a fine-grained corona mineral assemblage of clinopyroxene (Cpx_{r}) + orthopyroxene (Opx_{r}) + amphibole (Amp_{r}) + plagioclase (Pl_{r}) + quartz (Qz_{r}) developed at the rim of granoblastic garnet, clinopyroxene, orthopyroxene, and amphibole. These retrograde minerals also show differences in composition from the peak minerals (Fig. S3A–D; Table S2). Quartz and albite show low apparent dihedral angles when in contact with granoblastic minerals (Fig. 2B), interpreted as a melt pseudomorph from partial melting (e.g., Meek et al., 2019).

4.1.2. Metagabbro B

Metagabbro B is partially-transformed into granulite preserving coarse-grained igneous plagioclase (~23 vol%), clinopyroxene (~9%), and accessory minerals (~1%) such as magnetite, ilmenite, zircon, and apatite (Fig. 2C–D and Fig. 3A). The igneous clinopyroxene shows evidence of recrystallization at the grain boundaries, and contains extensive and fine-grained amphibole lamellae (Fig. 2E). The igneous clinopyroxene is augite-diopside with Ca of 0.78–0.89 apfu and X_{Mg} of 0.54–0.59 (Fig. 3B and Fig. S3E). The igneous plagioclase shows recrystallization as well, preserving a labradorite composition with X_{An} [= Ca/(Ca+Na+K)] of 0.53–0.65 in the former plagioclase core (Fig. 3D and Fig. S3F). These igneous relics are partially resorbed and locally replaced by metamorphic minerals, including plagioclase (~28 vol%), amphibole (~22%), quartz (~5%), biotite (~5%), garnet (~5%), orthopyroxene (~1%), and clinopyroxene (~1%). Most of the metamorphic minerals occur as a fine-grained multi-layered corona at the boundary between igneous clinopyroxene and plagioclase relics. From igneous clinopyroxene (or pseudomorph) outward, the corona contains (a) intergrown metamorphic amphibole + quartz ± orthopyroxene ± clinopyroxene ± biotite, (b) metamorphic plagioclase, (c) metamorphic garnet, and finally igneous plagioclase with individual metamorphic garnet grains (Fig. 2C and Fig. 4A).

Two groups of metamorphic garnet have been identified on the basis of composition and texture. Most of the garnet grains (Grt_{HTE}, i.e., garnet with high trace element) in the corona and individual garnet grains are compositionally homogeneous in major elements (Fig. 3E–H and Fig. S3G) with relatively low Ca and high Fe ($\text{Alm}_{65}\text{Prp}_{13}\text{Grs}_{19}\text{Sps}_{2}$), and are enriched in trace elements (Fig. 4A). The second garnet type (Grt_{LTE}, i.e., garnet with low trace element) is distributed outside the corona, and is compositionally zoned (Fig. 3E–H and Fig. S3G) with higher Ca, lower Fe ($\text{Alm}_{57\text{–}62}\text{Prp}_{11\text{–}13}\text{Grs}_{23\text{–}30}\text{Sps}_{2}$), and contains very low HREE+Y (Fig. 4A).

The intergrowth of plagioclase and quartz and the interstitial monomineralic K-feldspar films present along grain boundaries (Grt_{HTE}, plagioclase and quartz) with low dihedral angles are interpreted as textures related to the crystallization of a former melt (Fig. 2F; Meek et al., 2019). More commonly, albite, quartz, and K-feldspar are present at the grain boundaries and interstices between garnet and other minerals (Fig. 2G–H), suggesting that an interconnected melt channel may have existed in the inter-granular boundaries.

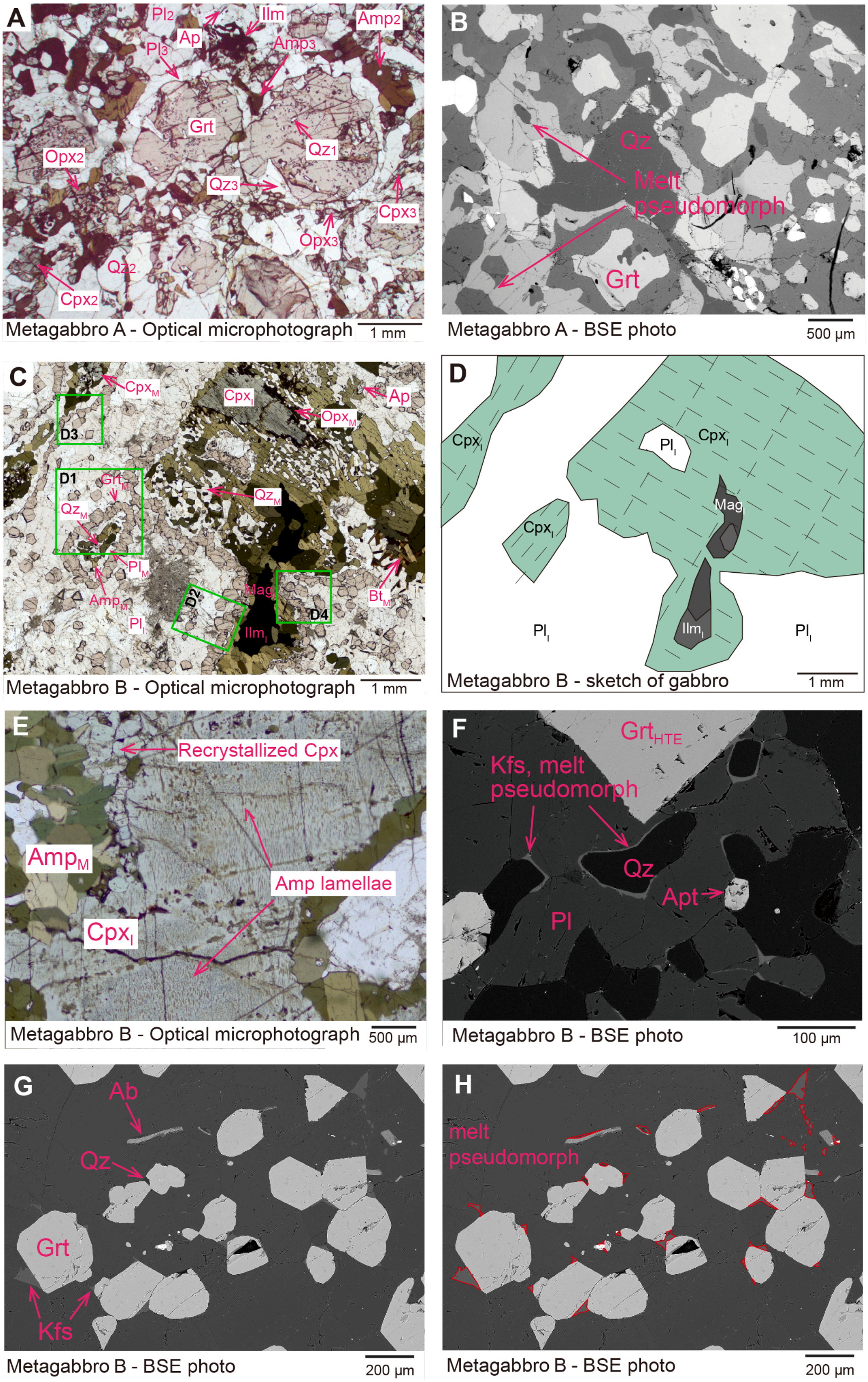

(caption on next page)

Fig. 2. Microphotograph of metagabbro A and B. (A) Metagabbro A is a mafic granulite, consisting of granoblastic minerals garnet, clinopyroxene, ±orthopyroxene, amphibole, plagioclase, and quartz. They were equilibrated at the peak stage, but were partially resorbed during retrogression and surrounded by a corona of clinopyroxene + orthopyroxene + amphibole + plagioclase + quartz. (B) BSE image of metagabbro A, quartz and albite show low apparent dihedral angles at the contact with granoblastic minerals, interpreted as melt pseudomorph. (C) Metagabbro B is a gabbro partially transformed into granulite, and preserves coarse-grained igneous clinopyroxene and plagioclase. These igneous relics were partially resorbed and are surrounded by multi-layered metamorphic corona. The corona—starting from igneous clinopyroxene relics — contains (a) intergrown amphibole + quartz ± orthopyroxene ± clinopyroxene ± biotite, (b) plagioclase layer, (c) garnet layer and finally to igneous plagioclase relics with individual garnet grains. Abbreviations: Amp_M, Qz_M, Pl_M, Grt_M—amphibole, quartz, plagioclase, garnet in metamorphic stage; Pl_I—plagioclase in igneous stage. (D) A sketch of the interpreted mineralogy of the protolith gabbro of metagabbro B. (E) Igneous clinopyroxene relics in metagabbro B show recrystallization at the edge, and extensive and fine-grained amphibole lamellae inside. (F) BSE image of metagabbro B, interstitial monomineralic K-feldspar films present along grain boundaries (Grt_{HTE}, plagioclase and quartz) with low dihedral angles, typically represent the former melt. The intergrowth of plagioclase and quartz blebs with K-feldspar fringes at the quartz-plagioclase boundary indicate a former rhyolitic melt composition. (G–H) K-feldspar, quartz, and albite occur as widespread melt pseudomorphs, which are present in the interstices between garnet and other minerals, suggesting an interconnected melt channel may have existed in the inter-granular boundary region. The melt pseudomorphs are highlighted in red color in Fig. 2H.

Three main stages of mineral equilibration are recognized based on mineral compositions and reaction textures: (i) the igneous stage, characterized by igneous relics, and two metamorphic (ii) prograde and (iii) peak stages. Multi-layered corona textures are often interpreted as being controlled by chemical potential gradients at constant *P–T* conditions (e.g., Ashworth and Sheplev, 1997; Joesten, 1977; Johnson and Carlson, 1990; Ogilvie and Gibson, 2017). The multi-layered corona textures (including Grt_{HTE} which is in contact with the melt pseudomorphs) are interpreted to have formed in the peak stage associated with partial melting. The corona-forming reaction in metagabbro B is inferred as (I = igneous, M = metamorphic):

$$Cpx_I + Pl_I + H_2O \rightarrow Amp_M + Pl_M + Qz_M + Grt_{HTE} \pm Opx_M \pm Cpx_M \pm Bt_M + \text{melt.} \quad (10)$$

This reaction occurred after the igneous stage; therefore, Grt_{HTE} is interpreted to have grown as a peritectic mineral in the presence of melt at peak conditions during regional metamorphism. Grt_{LTE} forms a low proportion of the overall garnet present and has extremely low trace element contents, indicating that it could have formed (possibly associated with some amphibole formation) during a prograde stage when only a small amount of igneous clinopyroxene was dissolved, and low amounts of trace elements were released. Moreover, Grt_{LTE} is often surrounded by the Grt_{HTE} (Fig. 4A), indicating that Grt_{LTE} grew earlier than Grt_{HTE}. Only the peak peritectic garnet (Grt_{HTE}) is considered for diffusion modeling.

4.2. *Metamorphic evolution*

4.2.1. *Metamorphic P–T conditions*

Metagabbro A displays a relatively homogeneous mineral assemblage on hand specimen scale at which the bulk composition is measured. The peak mineral assemblage (except garnet) also shows relatively homogeneous compositions (Fig. S3A–D; Table S2), indicating an absence of overprinting of peak mineral compositions. Therefore, the XRF bulk-rock composition and the average peak mineral compositions are appropriate to evaluate metamorphic *P–T* conditions using phase equilibrium modeling (Table S1). Because metagabbro B is partially transformed into granulite, only relatively homogeneous domains with metamorphic minerals were considered to generate reactive bulk compositions (Lanari and Engi, 2017; see EPMA_map2.mat in Zenodo repository), which was used to evaluate the metamorphic *P–T* conditions. Average peak mineral compositions were used for *P–T* estimation as no later overprinting of the peak metamorphic assemblage was observed in metagabbro B.

Phase equilibrium modeling was applied for metagabbro A and B, with both $T–M_{H2O}$ and *P–T* diagrams. For metagabbro A, a $T–M_{H2O}$ diagram was generated with H_2O ranging from 0 to 1.5 wt% (M_{H2O} ranging from 0 to 1) (Fig. S4A). The measured peak mineral compositions of X_{Grs} and X_{Prp} in the garnet inner rim (0.26; 0.14) and X_{An} in the granoblastic plagioclase (0.45–0.49) are predicted in the peak assemblage (Grt–Cpx–Amp–Ilm–Pl–Qz–Melt) field, constraining a suitable M_{H2O} range of 0.75–0.98. A middle M_{H2O} value of ~ 0.9 (1.35 wt% H_2O) was selected for the subsequent *P–T* equilibrium phase diagram. In the *P–T* diagram (Fig. S4B), the above peak metamorphic mineral assemblage is predicted to be stable in a large *P–T* range of 0.3–1.0 GPa and 720–870 °C. The measured X_{Grs} and X_{Prp} in the garnet inner rim (0.26; 0.14), and average X_{An} in plagioclase (0.47) constrain peak conditions of 0.8 GPa and 800 °C. The observed garnet proportion (15 vol%) isopleth is close to these *P–T* conditions. Orthopyroxene is predicted to be stable at slightly lower pressure than the peak stage, however, the measured X_{Mg} in orthopyroxene (0.41–0.43) is consistent with the temperature conditions of the modeled peak stage. This suggests that the orthopyroxene may have formed during the initial isothermal decompression stage. The interpreted retrograde corona assemblage (Cpx–Opx–Amp–Pl–Qz–Ilm–Melt) lies in the *P–T* range of 0.2–0.6 GPa and 725–820 °C, implying a further decompression-dominant *P–T* path.

For metagabbro B, a $T–M_{H2O}$ diagram was generated with H_2O ranging from 0 to 1.5 wt% (M_{H2O} ranging from 0 to 1) (Fig. S4C). The observed peak metamorphic assemblage is stable in the Grt–Cpx–Opx–Amp–Bt–Ilm–Pl–Qz–Melt field, constraining a suitable M_{H2O} range of 0.20–0.85. A middle M_{H2O} value of ~0.52 (0.79 wt% H_2O) was selected for the subsequent *P–T* equilibrium phase diagram for peak metamorphic stage. In the *P–T* diagram (Fig. S4D), the above peak metamorphic mineral assemblage is predicted to be stable in a *P–T* range of 0.4–0.85 GPa and 725–810 °C. The measured X_{Prp} in homogeneous garnet (Grt_{HTE}, Prp_{13}), X_{An} in metamorphic plagioclase (0.40–0.46), X_{Mg} in orthopyroxene (0.40–0.41) and X_{Mg} in amphibole (0.37) are plotted in the peak assemblage field, further constraining the peak *P–T* conditions to 0.6–0.8 GPa / 775–810 °C. The modeled X_{Grs} compositions in garnet at peak conditions is 0.21, which is close to Grt_{HTE} (Grs_{19}). The observed garnet proportion (7 vol%) isopleth is close to these *P–T* conditions. Under these conditions, ~10 vol% of rhyolitic melt is predicted to be stable (Table S1, No. 11), which is consistent with the observation of melt pseudomorphs (Fig. 2F–H). The absence of leucosomes (Fig. S1D) also indicates that this melt was not segregated in metagabbro B. A second equilibrium phase diagram was calculated for the prograde stage (Fig. S4E) using a near anhydrous bulk composition (M_{H2O} = 0.07 wt%, see section 4.2.2, water budget content in igneous stage). The measured range of compositions of X_{Alm} and X_{Grs} in the Grt_{LTE} ($Alm_{58–62}Grs_{23–27}$) plot in the Cpx–Grt–Opx–Bt–Kfs–Ilm–Pl–Qz field and fall within a *P–T* range of 0.3–0.5 GPa and < 800 °C, indicating possible conditions under which the Grt_{LTE} could have formed. This supports the interpretation that the Grt_{LTE} may have formed during the prograde stage (see section 4.1.2).

4.2.2. *Water budget during metamorphism*

The metagabbros A and B are identical in bulk-rock composition, peak metamorphic *P–T* conditions, and metamorphic age (Supplementary Results 2.1; Fig. S5; Table S3), suggesting they share the same igneous origin and record the same regional metamorphic event. Despite a comparable tectonic evolution, metagabbro A and B show different textures, the latter characterized by the preservation of magmatic relicts. The corona texture in metagabbro B is interpreted to form from relatively sluggish inter-crystalline diffusion under fluid-undersaturated

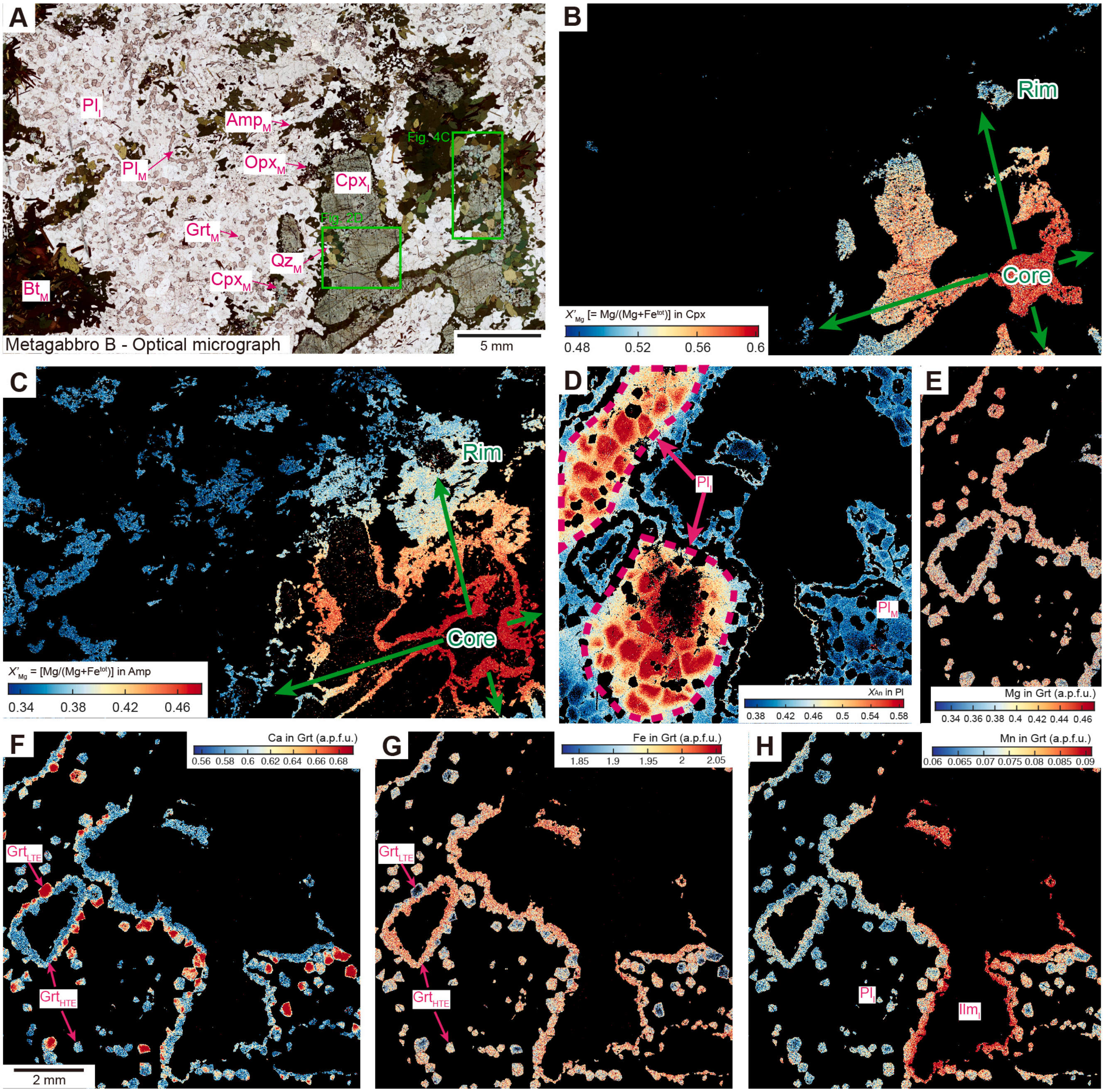

Fig. 3. Optical imaging and microprobe compositional maps of metagabbro B. (A) Optical micrograph of metagabbro B, the mapping area of Fig. 3B–C. (B) Map of X'_{Mg} [= Mg/(Mg + Fe^{tot})] in clinopyroxene. (C) Map of X'_{Mg} in amphibole. (D) Map of anorthite content (X_{An}) in plagioclase. The plagioclase interiors (enclosed by the pink dashed lines) show higher X_{An}, suggesting they may be compositions preserved in igneous relics. (E–H) Maps of Mg, Ca, Fe, and Mn content in garnet, in atoms per formula unit (apfu). The optical microphotograph for this mapping area is shown in Fig. 2C. Some garnet grains (Grt_{LTE}) show zoned chemical compositions of higher Ca, lower Fe, and lower trace element (Fig. 4A), interpreted as growth during prograde metamorphism; the other garnet grains (Grt_{HTE}) show homogeneous composition with lower Ca higher Fe, and higher trace element, interpreted as growth during peak conditions. See Fig. 4A and Fig. S4E for evidence from texture and phase equilibrium modeling.

conditions (e.g., Carlson, 2010; Gaidies et al., 2017), preserving metastable igneous phases. Therefore, different fluid conditions are inferred to control the textures developed in these samples.

The water budget was calculated for metagabbro A and B to determine the water content changes during the transition from the igneous to the peak metamorphic stage (see section 3.2.2). In addition, the water content estimated from T–M_{H2O} phase diagrams that stabilizes the peak mineral assemblage (Fig. S4A and C) was considered as an alternative water budget result (see below).

The protolith of metagabbro B is considered near-anhydrous based on the assumption that it only contains nominally anhydrous minerals, such as clinopyroxene and plagioclase. Hydrous minerals such as hornblende and biotite in metagabbro B usually occur as metamorphic corona around igneous relics. Additionally, the color of hornblende in metagabbro B is more consistent with green metamorphic hornblende rather than brown igneous hornblende (e.g., Miyashiro & Shido, 1980; Ross & Elthon, 1997). Measurement of OH in magmatic clinopyroxene relics by Fourier-transform infrared spectroscopy (FTIR) (Supplementary Results 2.2; Fig. S6A; Table S4) constrain a minimum water content of ~ 73 µg/g in metagabbro B during the igneous stage (Table S5). The

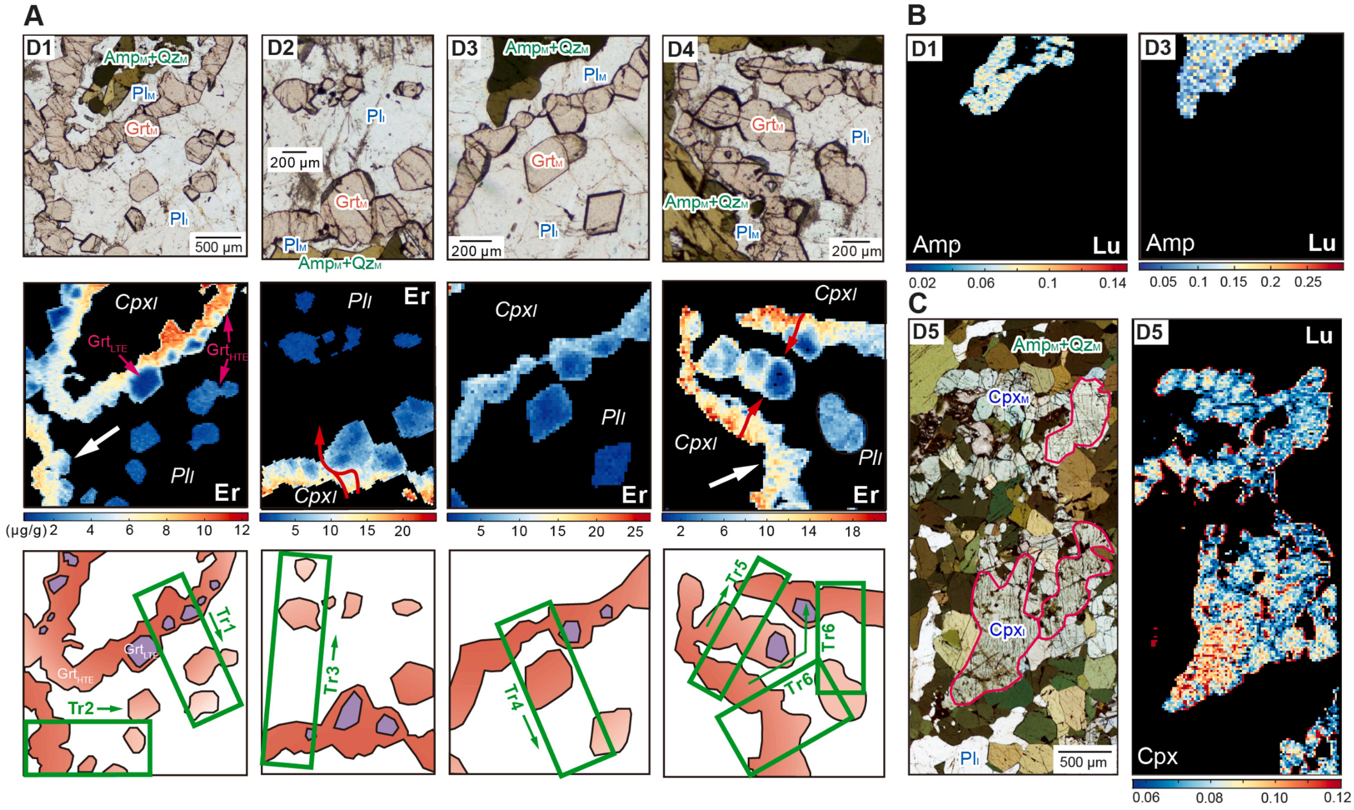

Fig. 4. Optical imaging and HREE+Y compositional mapping for minerals in metagabbro B. (A) Optical image, quantitative Er (as example of HREE+Y) compositional maps of garnet, and sketch figure of domain 1 to 4 (D1–4 in Fig. 2C) in metagabbro B. Purple Grt_{LTE} is often surrounded by the red Grt_{HTE}, indicates the Grt_{LTE} formed during an earlier prograde stage (see Fig. S4E for results of phase equilibrium modeling). A systematic decrease of HREE+Y content across garnet corona from Cpx_I to individual garnet grains in Pl_I, with a direction perpendicular to the annuli. Relatively higher Er filling can be seen in the interstices of the crystals (marked by the red curves with arrows), which may represent the flow channel of the melt and indicate the HREE+Y was still being supplied as the reaction was continuous. The white arrows highlight HREE+Y gradient across a single garnet grain. Six elemental profiles were extracted in XMapTools along six transects Tr1 to Tr6, these HREE+Y data are given in Zenodo repository. (B) Quantitative Lu (as example of HREE+Y) compositional maps of amphibole in D1 and D3 domains. (C) Optical image, quantitative Lu (as example of HREE+Y) compositional maps of clinopyroxene. HREE+Y content is higher in igneous clinopyroxene than that in metamorphic recrystallized clinopyroxene.

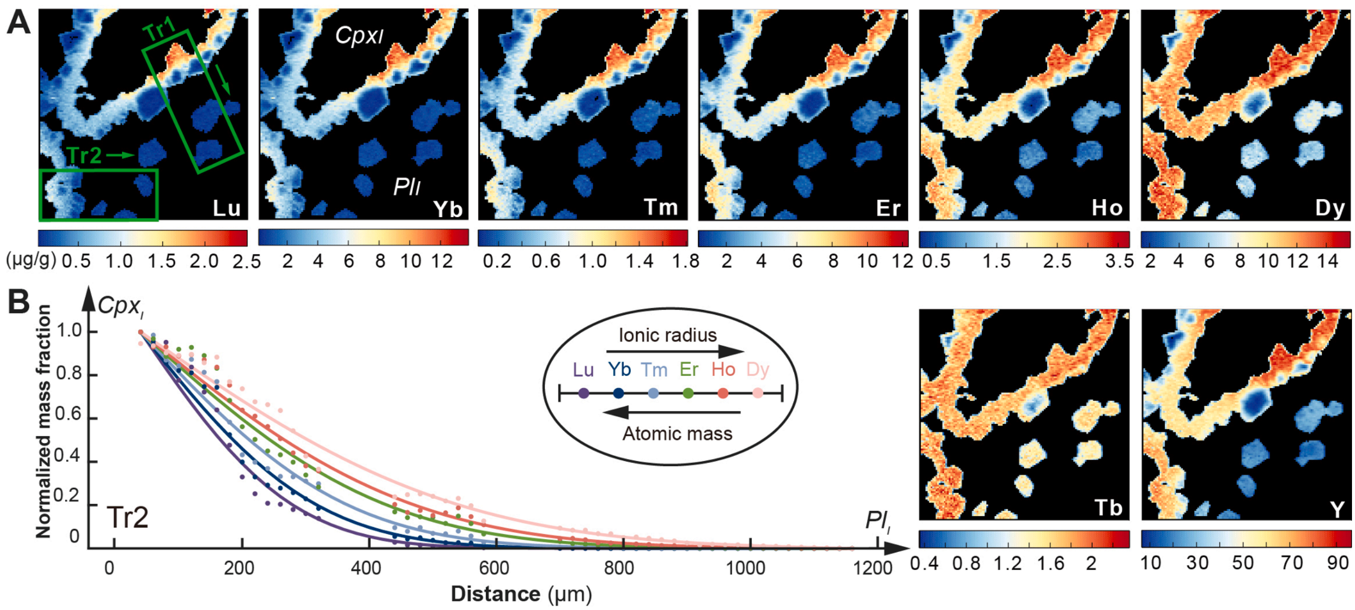

Fig. 5. HREE+Y compositional mapping and extracted HREE compositional profiles for garnet in metagabbro B. (A) Quantitative HREE+Y compositional maps of garnet in domain 1 (Lu, Yb, Tm, Er, Ho, Dy, Tb, Y expressed in µg/g). (B) Interpolated profiles of HREE data in Tr2 normalized as 0 to 1. Interpolated profiles were based on these measured data (colorful solid dots) and the mass fraction of each element was normalized to 0–1 to compare the relative diffusivities among HREE. These interpolated profiles show an increasing curvature with the atomic mass of HREE, suggesting a decreasing diffusion rate.

magmatic protoliths were essentially anhydrous, and hydration by an external aqueous fluid during metamorphism is required to crystallize the hydrous minerals amphibole and biotite. Considering the minimum amount of water stored in the samples, i.e., sum of H_2O in hydrous minerals and nominally anhydrous minerals (e.g., garnet, Fig. S6B; Table S4), an addition of ~ 0.78 wt% H_2O prior to or during metamorphism is estimated for metagabbro B to stabilize the above hydrous minerals in the observed peak mineral assemblage (Table S5). This water content is consistent with what estimated from T–M_{H2O} phase diagram (Fig. S4C, 0.79 wt% H_2O). Therefore, the incomplete equilibration observed in metagabbro B is interpreted as due to a limited supply of water.

For metagabbro A, the igneous stage was also considered as essentially anhydrous. Peak metamorphic minerals were partially consumed during retrograde metamorphism (Fig. 2A and Fig. S4B), preventing the water budget for the peak metamorphic assemblage from being directly constrained by the preserved minerals. The T–M_{H2O} phase diagram for metagabbro A suggests a water content of 1.35 wt% H_2O at peak conditions (Fig. S4A). Therefore, the peak mineral assemblage of metagabbro A is interpreted as having formed under water conditions sufficient to completely transform the igneous minerals into a fully metamorphic assemblage (1.35 wt%).

In summary, the infiltration of H_2O in metagabbro A and B at ~ 800 °C / 0.8 GPa catalyzed metamorphism and partial melting reactions. Metagabbro A was completely re-equilibrated at peak stage with 1.35 wt % H_2O, whereas metagabbro B was only partially re-equilibrated (containing 0.78 wt% H_2O) with the formation of metamorphic corona in the presence of ~ 10 vol% rhyolitic melt. Both metagabbro samples formed under H_2O-undersaturated conditions, the corona texture in metagabbro B is interpreted to form from relatively sluggish inter-crystalline diffusion under even more fluid-undersaturated conditions.

4.3. Gradients in mineral compositions

Major and minor elements show chemical gradients at different scales. At the centimeter scale (Fig. 3A–C), the coarse-grained igneous clinopyroxene and the fine-grained metamorphic amphibole corona in metagabbro B retain consistent X'_{Mg} [= Mg/(Mg+Fe^{tot})] gradients decreasing from core to the rim with constant partition coefficient for Fe^{2+}/Mg ($\ln K_d = 0.43$) between clinopyroxene and amphibole (Fig. S7). This pattern suggests local equilibrium conditions during amphibole growth with limited mass transport from the reaction site (see $\ln K_d$ value in Molina and Poli, 1998). This unique example shows frozen-in chemical potential gradients of FeO and MgO not perpendicular to the corona layering. At the millimeter scale, garnet (Grt_{HTE}) in metagabbro B shows a MnO content decreasing from igneous ilmenite to igneous plagioclase (Fig. 3H), suggesting a chemical potential gradient of MnO perpendicular to the corona layer.

Trace element distribution varies between different minerals. HREE+Y compositional maps of four distinct areas within the same thin section of metagabbro B show that garnet hosts the vast majority of HREE+Y (Fig. 4 and Fig. S8), and show a systematic decrease of HREE+Y content in garnet (Grt_{HTE}) at the transition from igneous clinopyroxene to igneous plagioclase, perpendicular to the coronal layering. As HREE+Y are relatively enriched in igneous clinopyroxene and significantly depleted in igneous plagioclase (Fig. 4C and Fig. S8E–F; Table S6), this trend possibly reflects a diffusion gradient driven by chemical potential (μ) gradients. In addition, igneous clinopyroxene relics show higher HREE+Y than metamorphic recrystallized diopside (Fig. 4C), requiring diffusion-out of these elements from the reaction site during metamorphism. The igneous clinopyroxene is considered as the main source of HREE+Y that were mainly incorporated by garnet, and to a lesser amount in amphibole, clinopyroxene, and orthopyroxene during metamorphism. Metamorphic plagioclase and biotite are virtually HREE+Y free (Table S6).

Trace element gradients across several garnet grains indicate a diffusion gradient driven by $\Delta\mu_{HREE+Y}$ from igneous clinopyroxene to igneous plagioclase. Diffusion is inferred to take place in the inter-granular medium in the presence of ~ 10 vol% rhyolitic melt in metagabbro B (Fig. 2F–H; Table S1, No. 11), and peritectic garnet (Grt_{HTE}) is interpreted to grow at peak conditions with the melt according to the observed texture (Fig. 2F). This assumption is discussed in detail in section 5.1. The conditions at which the HREE+Y diffusion gradient formed can be assessed using the six compositional profiles of normalized mass fraction extracted from the compositional maps. They show an increasing curvature with increasing atomic mass of HREE (Fig. 5 and Fig. S9), suggesting a decreasing diffusion rate with atomic mass. This trend is inconsistent with intra-granular diffusion in garnet, but is instead consistent with those observed in the melt, strongly supporting the above hypothesis that the HREE+Y gradients were formed by diffusion in the inter-granular melt and captured/inherited by garnet growth nearby (see section 5.1 for detailed discussion). Therefore, we propose that the observed HREE+Y compositional gradient across several garnet grains reflects different reactive bulk compositions in the vicinity of each garnet grain during its growth. These local reactive bulk compositions, including major and trace elements, were controlled by dissolution of igneous clinopyroxene and plagioclase involved in the partial melting reaction and by element transport in the inter-granular melt.

4.4. Mass balance calculation for HREE+Y

The mass balance of HREE+Y and their partitioning during metamorphism were calculated (Table S7). In the following, Lu was selected as an example to explain the calculation method. For the igneous stage, the previous volume proportion of each igneous mineral was estimated from the current textures in the rock (e.g., Fig. 2D). HREE+Y in igneous clinopyroxene was considered unknown and recovered by mass balance calculation because the HREE+Y were released and diffused from igneous clinopyroxene during dissolution, exsolution, and recrystallization (Fig. 2E and Fig. 4C). The amounts of HREE+Y in other igneous minerals (Pl, Mag, Ilm, Zrn, Ap) were considered unmodified and taken from the average measured values. The measured Lu mass fraction in bulk rock is 0.33 μg/g (Table S1), and the average Lu mass fraction in igneous clinopyroxene was calculated to be 0.30 μg/g according to Eq. (3) (Table S7). As a verification, seventy-three laser single-spot analyses were measured on igneous clinopyroxene. These analyses yielded mainly a range of Lu mass fractions from 0.06 to 0.20 μg/g, with eight analyses outside of that range (0.21 to 0.33 μg/g; Table S6). Widespread low-Lu compositions and rarely preserved high-Lu components of igneous clinopyroxene agree with the mass balance calculations and our assumption above.

For the metamorphic stage, the average Lu mass fraction in the sum of the metamorphic minerals was calculated to be 0.14 μg/g according to Eq. (4) based on the difference between Lu mass fraction in the bulk rock and in the igneous relics. The partitioning of the average Lu mass fraction in the metamorphic garnet, amphibole, clinopyroxene, orthopyroxene, and remaining melt (equilibrated with the metamorphic minerals, Fig. 6A) was calculated to be 1.60, 0.18, 0.06, 0.02, and 0.08 μg/g (Table S7), respectively, according to Eq. (5) and their partition coefficients at granulite facies conditions (Nehring et al., 2009). The measured average values of Lu mass fraction in garnet, amphibole, clinopyroxene, and orthopyroxene are 1.33, 0.19, 0.07, and 0.03 μg/g, respectively (Table S6). These measurements are compatible with the calculation results, which further support the validity of the mass balance and (local) equilibrium partitioning of elements between metamorphic phases. In order to recover the HREE+Y diffusion profile in the initial melt (before HREE+Y incorporation in newly grown metamorphic minerals, Fig. 6A), the average Lu mass fraction in the initial melt and its ratio to the average Lu mass fraction in garnet were also calculated. The average Lu mass fraction in the initial melt was calculated to be 2.10 μg/g according to Eq. (3). A constant coefficient of Lu

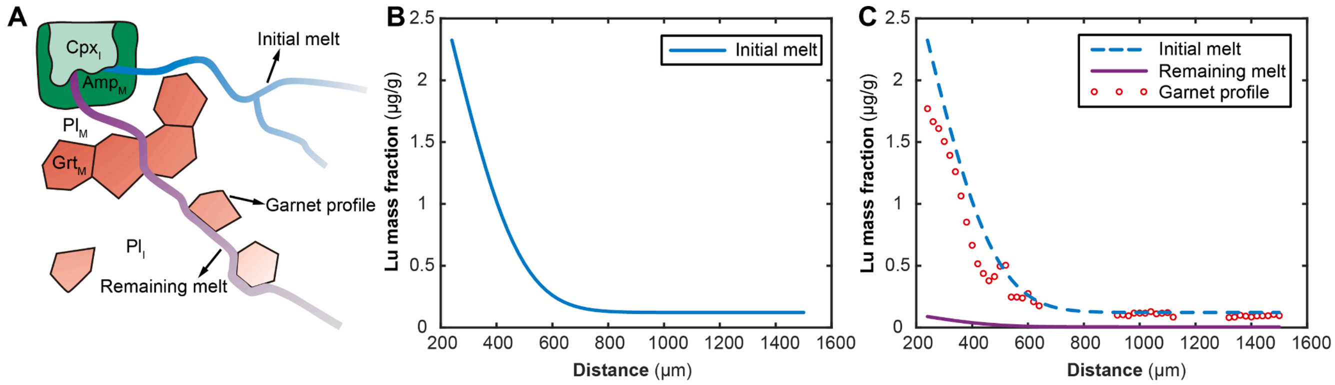

Fig. 6. Schematic diagram showing the relationship of HREE+Y (Lu as example) between the initial melt, the residual melt, and across several garnets. HREE+Y gradients in the initial melt and in the remaining melt were recovered from those across several garnets by mass balance calculation. HREE+Y across several garnets can be used as a proxy for recovering HREE+Y in the initial/remaining melt and for further diffusion modeling. (A) Cartoon depicting the relationship of HREE+Y gradients in garnet, initial melt, and remaining melt. At the beginning of the metamorphic reaction, HREE+Y are released from igneous clinopyroxene and diffuse in the initial melt; afterwards, garnets (and other minerals) grow and absorb HREE+Y from the neighboring melt. Most of the HREE+Y gradient is hosted by the garnet, and only a small amount of HREE+Y gradient is in the remaining melt. (B) Recovered HREE+Y diffusion profile in initial melt. (C) HREE+Y diffusion profile in initial melt, remaining melt, and the measured garnet data profile. The measured garnet data profile is selected from transect 1, the diffusion profiles in initial and remaining melt were estimated based on those in garnet following mass balance calculation.

average mass fraction between initial melt and garnet that follows mass balance is calculated to be 1.3, which is controlled by partition coefficients and volume proportions of metamorphic minerals and melt. Therefore, the HREE + Y profile composition (in mass fraction) in the initial melt can be recovered by the HREE+Y profile composition in garnet multiplied by their constant coefficients (e.g., 1.3 for Lu; Fig. 6B–C). The HREE+Y profile composition in the remaining melt can be calculated by HREE+Y profile composition in garnet divided by its partition coefficient $K_{\mathrm{d\,HREE+Y}}^{\mathrm{garnet/melt}}$ (e.g., 20 for Lu, Nehring et al., 2009; Fig. 6C). Therefore, the HREE+Y compositions recorded by several individual garnet grains across the diffusion profile are used (i) to test the hypothesis that the current zoning in garnet reflects the diffusion within the initial inter-granular melt and (ii) as a proxy to estimate the timeframe of diffusion within the initial inter-granular melt, because multiplying by the above fixed constant coefficient (e.g., 1.3 for Lu) will result in the same timescale obtained by diffusion modeling.

4.5. Diffusion modeling

HREE+Y diffusion in the melt was modeled using two different boundary conditions, i.e., a fixed boundary model and a moving boundary model (Fig. 7). The fixed boundary model uses the HREE+Y diffusion profile compositions in garnet, and treats the two ends of the profile as fixed boundaries. It enables quantitative diffusion modeling based on measured compositions; however, it neglects the effect of Cpx$_I$ consumption during metamorphic reaction progress. The moving boundary model simulates the process of the Cpx$_I$–Melt interface gradually moving as the Cpx$_I$ reacts. Whilst it more closely reflects the natural process, it cannot be inverted to obtain a duration due to the lack of constraints on the additional parameters (see below).

4.5.1. HREE+Y diffusion modeling in melt using a fixed boundary model

Quantitative modeling of HREE+Y diffusion in the inter-granular melt was used to calculate the diffusion-controlled process in metamorphic reactions. The temperature T is fixed at 800 °C according to the metamorphic peak conditions (Fig. S4D). Six chemical profiles for Lu, Yb, Er, Ho, Dy, and Y were extracted from compositional maps in metagabbro B for diffusion modeling (Fig. 8). Maximum contents are variable from profile to profile, indicating variations in the distance from the reaction site, or in the amount of metamorphic amphibole, and/or in the initial content of HREE+Y in igneous clinopyroxene. However, after shifting profiles along the x-axis, the shapes of the profiles are identical, suggesting a similar diffusion-controlled process (Fig. 8). A global inversion was performed to retrieve the diffusion time t, considering each profile for each of the six elements. The diffusivities D_0 and E_a of HREE+Y in melt with a water content of ~6.2 wt% H_2O (Table S8) are

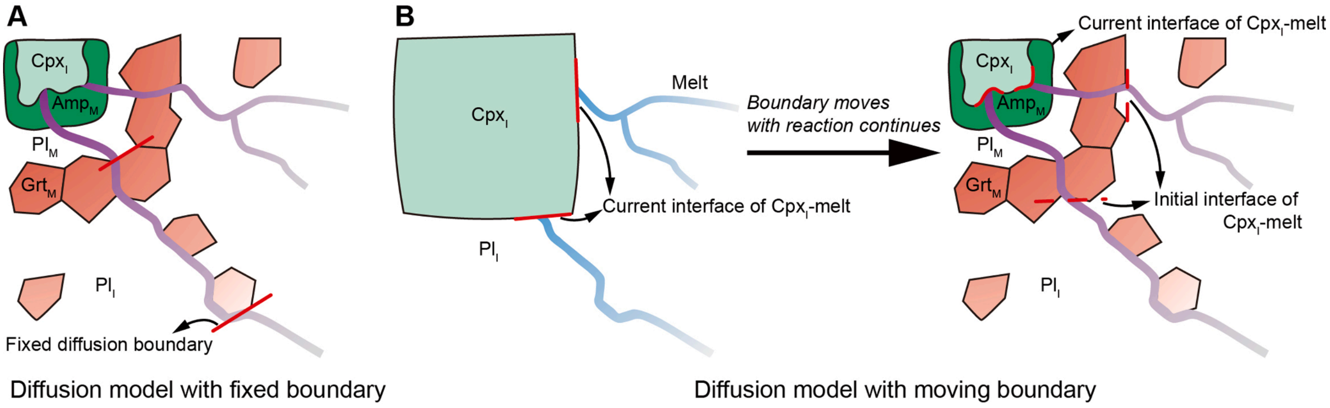

Fig. 7. Cartoon depicting diffusion model with different boundary conditions. (A) HREE+Y gradients inherited by several garnet grains were used as a proxy for diffusion modeling, the two ends of the profile were treated as fixed boundaries. (B) Diffusion modeling with moving boundary model. The Cpx$_I$-Melt interface is gradually moving with consumption of Cpx$_I$. Note that the color of the initial melt and the remaining melt are consistent with those in Fig. 6.

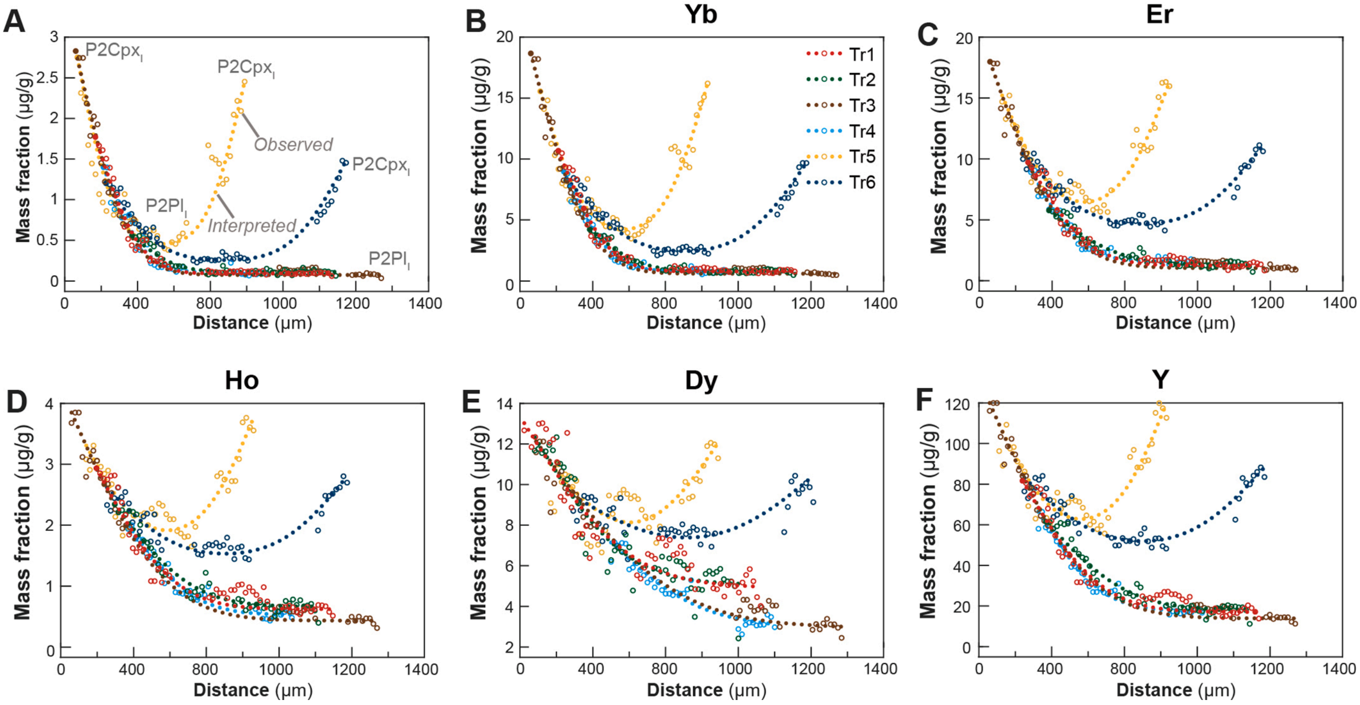

Fig. 8. Measured data across garnet grains and interpreted profiles from all transects in each element. Circles indicate measurements and dotted lines show the interpreted profiles which represent the diffusion profiles in the melt. The six profiles were shifted along their *x*-axis, showing that they share a similar trend. P2Cpx$_I$ indicates "proximal to igneous clinopyroxene relics", P2Pl$_I$ represents "proximal to igneous plagioclase relics". "Tr" means "transect". Tr1–Tr4 show unilateral diffusion from igneous clinopyroxene on one side and to igneous plagioclase on the other side; Tr5–Tr6 show bilateral diffusion from igneous clinopyroxene at both ends and to the igneous plagioclase in the middle (see Fig. 4A for textures).

selected from Holycross and Watson (2018), according to the calculated water content in the melt from the phase equilibrium modeling (6.3 wt% H_2O, Table S1, No. 11) of metagabbro B at peak metamorphic conditions. This melt composition is very similar to the melt composition in Holycross and Watson (2018) (Fig. S10), indicating that the experimental diffusivities are applicable for the diffusion modeling of partial melts in metagabbro B. Diffusivities from Holycross and Watson (2018) with ~4.1 wt% H_2O were also used for comparison. The algorithm matches the observed and modeled diffusion profiles assuming a step function as the initial profile, which represents the initial grain boundary between magmatic clinopyroxene and plagioclase (Fig. 9). An optimal t value of 8.4 (+5.4/-3.3) days was obtained (Fig. 9). The second set of experimental diffusivities results in an optimal t value of 34.6 (+22.3/-13.6) days, indicating that the uncertainties in estimating the water content in melt will not significantly affect the final timescale.

4.5.2. HREE+Y diffusion modeling in melt using a moving boundary model

The clinopyroxene–melt interface will move towards the dissolving igneous clinopyroxene (Fig. 7). Therefore, a moving boundary should be considered for diffusion modeling according to Eq. (8). However, additional parameters are required when considering a moving boundary, e.g., the HREE+Y mass fraction in igneous clinopyroxene, and the volume fraction of clinopyroxene, amphibole, clinopyroxene, plagioclase, orthopyroxene, garnet, and melt, which make it impossible to obtain an optimal time from these models. Therefore, an exploratory diffusion model with a moving boundary was implemented instead to show the HREE+Y diffusion response in the melt for different timescales.

The results of the diffusion modelling are shown using Lu as an example. Amphibole, which forms the first layer of the metamorphic corona, has relatively higher HREE+Y contents; therefore, amphibole incorporates moderate HREE+Y alongside garnet during the dissolution of igneous clinopyroxene. Therefore, a fixed Lu content from amphibole was subtracted from the dissolution of clinopyroxene and the remaining Lu content represents the total value available for diffusion in the melt. All parameters in the modeling were taken from the average values in Table S7. Fig. 10A shows an initial condition, with a Lu mass fraction in igneous clinopyroxene of 0.30 µg/g, and Lu mass fraction in melt of 0 µg/g (at the beginning of melt production and before element partitioning). Fig. 10B shows the diffusion profile of Lu in the melt after different durations from 1 day to 100 years during which 400 µm of igneous clinopyroxene was consumed, resulting in various dissolution rates. At the end of the model, the 400 µm igneous clinopyroxene has completely dissolved and its place has been taken by the melt. The clinopyroxene–melt interface moved towards the left (dotted and solid red lines in Fig. 10B) following the dissolution of igneous clinopyroxene. The results show that the diffusion profiles flatten out with decreasing diffusion rate, i.e. increasing diffusion timescales. The diffusion profiles fit timescales of 1 day to 1 year, constraining the timescales of less than a year for the metamorphic reactions in metagabbro B.

5. Discussion

5.1. Diffusion of HREE+Y in inter-granular melt

All six compositional profiles across multiple garnet grains show a decreasing gradient from the margin close to igneous clinopyroxene to the area close to plagioclase (Figs. 5 and 8). A key assumption for the application of diffusion chronometry in this study is that HREE+Y diffusion took place in the inter-granular medium filled with melt and then were inherited by garnet during their growth. There are three pieces of evidence to support this assumption.

(i) The melt pseudomorphs widely retained at the boundaries and interstices between mineral grains, suggesting that the existence of an interconnected melt channel within the inter-granular medium (Fig. 2F–H).

(ii) The HREE+Y gradients are not confined to a single garnet grain, but rather occur across several individual garnet grains. Such HREE+Y

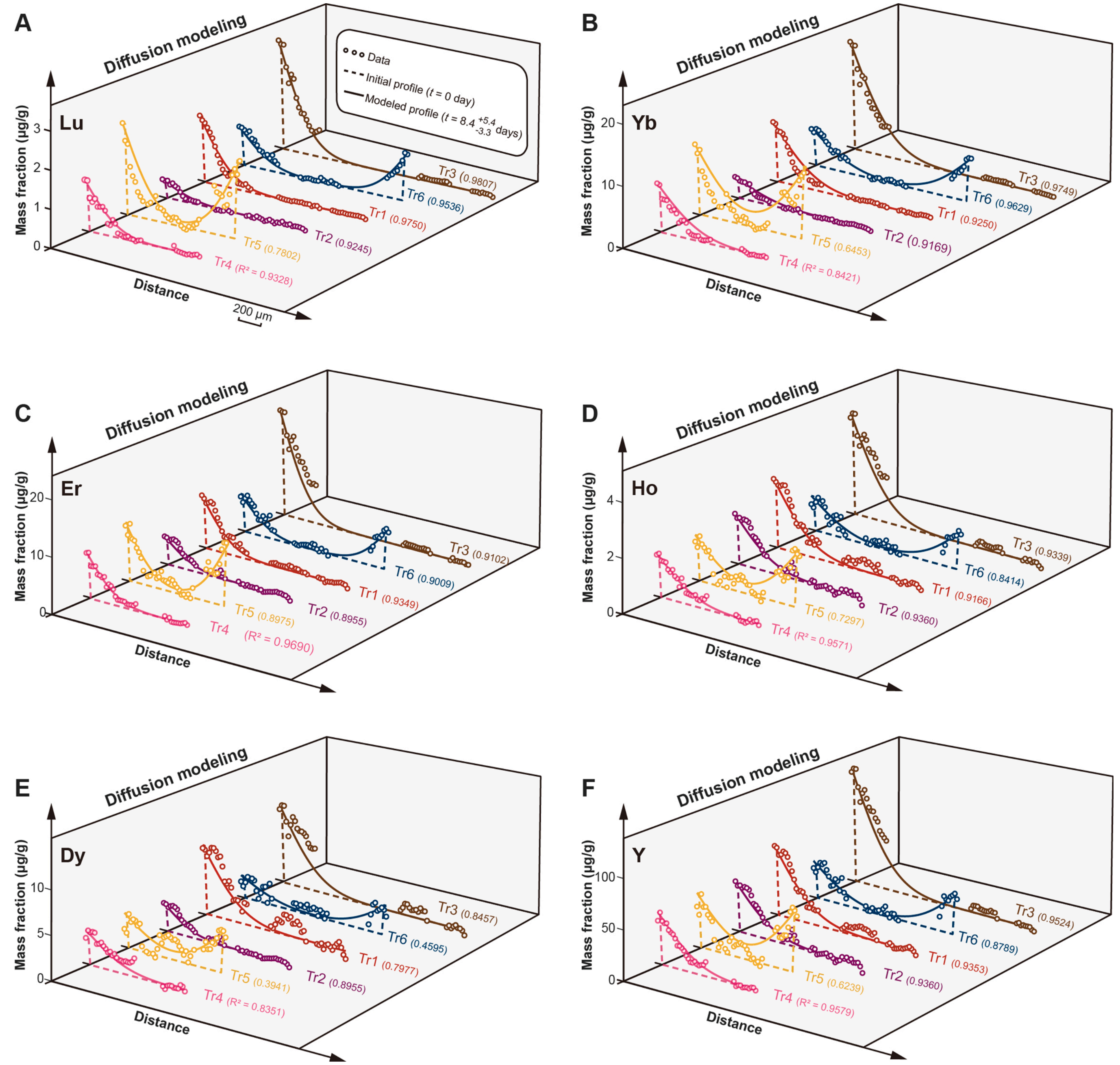

Fig. 9. Global diffusion modeling results of HREE+Y using experimental diffusivities. The dashed lines represent the assumed initial profiles at $t = 0$ day (step function). The solid lines show the modeled profile at $t = 8.4$ (+5.4/-3.3) days for multi-elements and multi-profiles together. R^2 means coefficient of determination.

gradients decrease within a single garnet grain (white arrows in Fig. 4A) and continue to decrease in the following garnet grains. HREE+Y gradients formed under equilibrium conditions can be controlled by Rayleigh fractionation within single garnet grains (Fig. 11A); whereas the scenario proposed here, requires HREE+Y transport and diffusion in the inter-granular medium to be recorded by the different garnet grains (Fig. 11B).

(iii) The comparison of the relative diffusion rates of HREE in garnet and in melt further supports this assumption. All six compositional profiles across several individual garnet grains show an increasing diffusion rate with decreasing atomic mass of HREE ($Lu_{175} \rightarrow Yb_{173} \rightarrow Tm_{169} \rightarrow Er_{167} \rightarrow Ho_{165} \rightarrow Dy_{162}$), or with increasing ionic radius (pm) of $HREE^{3+}$ ($Lu_{85} \rightarrow Yb_{86} \rightarrow Tm_{87} \rightarrow Er_{88} \rightarrow Ho_{89} \rightarrow Dy_{91}$) (Fig. 5B). Experimental and modeling studies of HREE diffusion in garnet proposed either indistinguishable diffusivity variations among the HREE (e.g., Bloch et al., 2020; Carlson, 2012a; Van Orman et al., 2002) or slightly increasing diffusivities with decreasing ionic radius (Rubatto et al., 2020; Tirone et al., 2005). Both results are inconsistent with the observed diffusion profiles (Fig. 5B). On the other hand, experimental studies of REE diffusion in melt are available for various compositions (rhyolitic, andesitic, basaltic, trachytic, phonolitic) and water contents (Behrens and Hahn, 2009; Holycross and Watson, 2016; Holycross and Watson, 2018; Koepke and Behrens, 2001). They all show a systematic increase of REE diffusivities with decreasing atomic mass ($D_{Lu} < D_{Yb} < D_{Tm} < D_{Er} < D_{Ho} < D_{Dy}$), which is consistent with the observed relative diffusion rates in metagabbro B (Fig. 5B). Holycross and Watson (2016) interpreted this negative correlation between diffusivities and atomic mass as related to the strength of the REE-O bond, which increases with atomic mass (Cicconi et al., 2013). Heavier elements experience a significant energy barrier that inhibits their mobility in the melt.

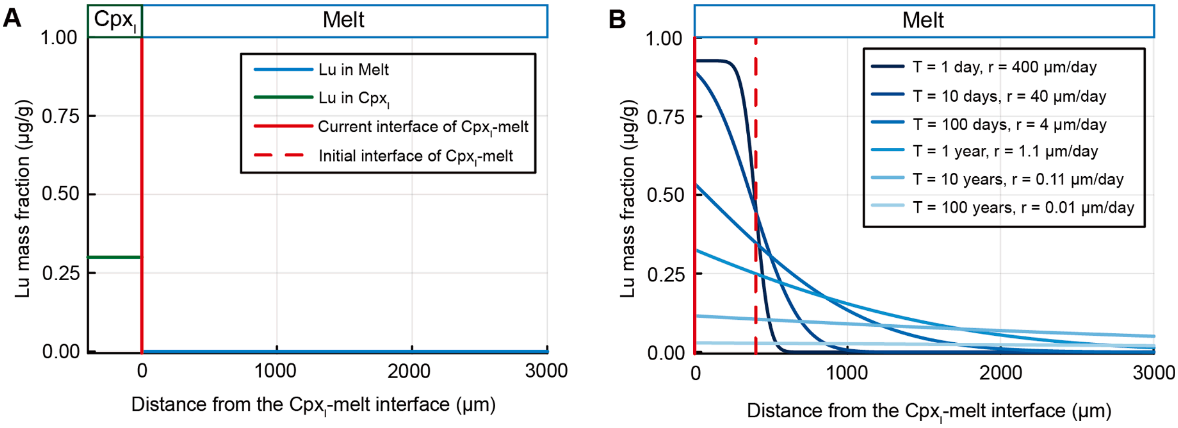

Fig. 10. Diffusion modeling with moving boundary model. (A) Initial conditions of Lu in igneous clinopyroxene and melt. (B) Diffusion profile of Lu in the melt during different timescales (from 1 day to 100 years) and dissolution rates (from 0.01 μm/day to 400 μm/day). The Cpx$_I$-melt interface is moving with the consumption of igneous clinopyroxene.

One might argue that such HREE+Y gradients could also be formed by Rayleigh fractionation across several individual grains through diffusion/transport in dry mineral boundaries, if the garnet grains grow sequentially from the inner to the outer part of the corona (Fig. 11C). This scenario could also form the observed relative trend/curvatures in the HREE gradients, i.e., $C_{Lu} > C_{Yb} > C_{Tm} > C_{Er} > C_{Ho} > C_{Dy}$ (C means curvature), but due to different mechanisms with our assumption (HREE diffusion in the inter-granular melt). For the Rayleigh fractionation model (Fig. 11C), the relative curvatures of HREE are controlled by their relative K_d, which increases with their atomic mass, i.e., $K_d^{Lu} > K_d^{Yb} > K_d^{Tm} > K_d^{Er} > K_d^{Ho} > K_d^{Dy}$ (e.g., Otamendi et al., 2002). An element with a higher K_d is more compatible in garnet, causing it to be depleted earlier in the system, thus showing a steeper mass fraction profile (higher curvature) in garnet. As for diffusion in the melt (Fig. 11B), the relative curvatures of HREE are determined by their relative diffusivities in the melt, which decrease with their atomic mass, i.e., $D_{Lu} < D_{Yb} < D_{Tm} < D_{Er} < D_{Ho} < D_{Dy}$. Elements with lower diffusivities would be slower to reach equilibrium, thus showing a higher curvature. However, there are several lines of evidence suggesting that this Rayleigh fractionation scenario is unlikely compared with our assumption of HREE+Y diffusion in the inter-granular melt.

(i) Such a scenario would produce a different HREE+Y gradient pattern from both the observed HREE+Y gradients and our assumption. For the observed HREE+Y gradients (Fig. 5B and Fig. S9) and our assumption (Fig. 11B), there is a part of "missing" HREE+Y in the gradients because these HREE+Y in melt were not absorbed by available garnet nearby. These "missing" HREE+Y may migrate with melt and be enriched in some garnet rims at a late stage. It can be seen that a relatively higher HREE+Y mass fraction is present in some of the garnet rims which form in the interstices between different garnet grains (red curves with arrows in Fig. 4A). This may represent the fate of the above mentioned "missing" HREE+Y between two garnet grains. On the other hand, for a scenario of HREE+Y controlled by Rayleigh fractionation across several garnets during their growth outwards from the corona (Fig. 11C), the HREE+Y gradients would rather retain the "constant" HREE+Y mass fraction on the garnet rims between the previous garnet and the next garnet (Fig. 11C), since garnet would grow and absorb HREE+Y continuously from corona outwards, and there are no other minerals present in between to incorporate HREE+Y. All the measured HREE+Y gradients across several garnet grains (Fig. 5B and Fig. S9) correspond with the HREE+Y pattern of Fig. 11B rather than Fig. 11C, which supports our assumption of HREE+Y diffusion in the melt, rather than a scenario of Rayleigh fractionation across several garnets.

(ii) Although both this Rayleigh fractionation scenario (Fig. 11C) and our assumption of HREE+Y diffusion in the melt (Fig. 11B) could produce the observed relative curvatures of HREE gradients under different mechanism (see above), their effects are very different. Holycross and Watson (2016) conducted detailed theoretical modeling to investigate how diffusivity effects and crystal/melt partitioning coefficient (K_d) effects compete to influence REE uptake in minerals. They extended the method of Watson and Müller (2009) to model the La/Lu fractionation process during clinopyroxene growth with a basalt melt at 1200 °C. Their results show that fractionation of REEs is modest for slow-growing crystals but significant when they grow very fast. They also demonstrate that the fractionation of REE during rapid crystal growth depends critically on their relative diffusivities rather than their relative partition coefficients. This study helps to rule out the possibility of Rayleigh fractionation across several grains and supports our hypothesis.

(iii) Finally, the scenario of Rayleigh fractionation across several individual grains would require each garnet to grow from the corona outwards (Fig. 11C). While this might be reasonable for the Grt 1 forming the corona, it is less realistic for the automorph grains located in the plagioclase matrix.

One might also question if garnets grew at or close to the position of previous igneous minerals, e.g., clinopyroxene, whether the HREE+Y gradients in garnets were simply inherited from the primary HREE+Y growth zoning of igneous clinopyroxene. Given that HREE+Y gradients in six transects from four maps at different angles show an identical and overlapping trend (Fig. 8), this scenario would require that the igneous clinopyroxene was an isometric crystal and contained identical concentrical growth zoning of HREE+Y in each grain, which is unlikely. Furthermore, this scenario cannot explain the source of HREE+Y in some individual garnets, which grew within igneous plagioclase, as there is a negligible amount of HREE in plagioclase.

The above discussion supports the assumption that HREE+Y gradients across several garnet grains record element diffusion in the inter-granular melt. However, garnet may have experienced intra-granular diffusion after growth. Intra-crystalline diffusion of HREE+Y in garnet is 7–9 orders of magnitude slower than in the melt (Carlson, 2012; Bloch et al., 2020) and 1–4 orders of magnitude slower than the major element diffusion in garnet and clinopyroxene (e.g., Bloch et al., 2020; Carlson, 2006; Carlson, 2012; Müller et al., 2013). The composition gradient in major and minor elements preserved in clinopyroxene (Fe-Mg), amphibole (Fe-Mg), and garnet (Mn) (Fig. 3B, C and H) indicates limited post-growth intragranular diffusion, possibly due to rapid cooling and/or insufficient structurally-bound water in minerals.

5.2. *Diffusion modeling*

Metamorphic reactions include interface-controlled and diffusion-

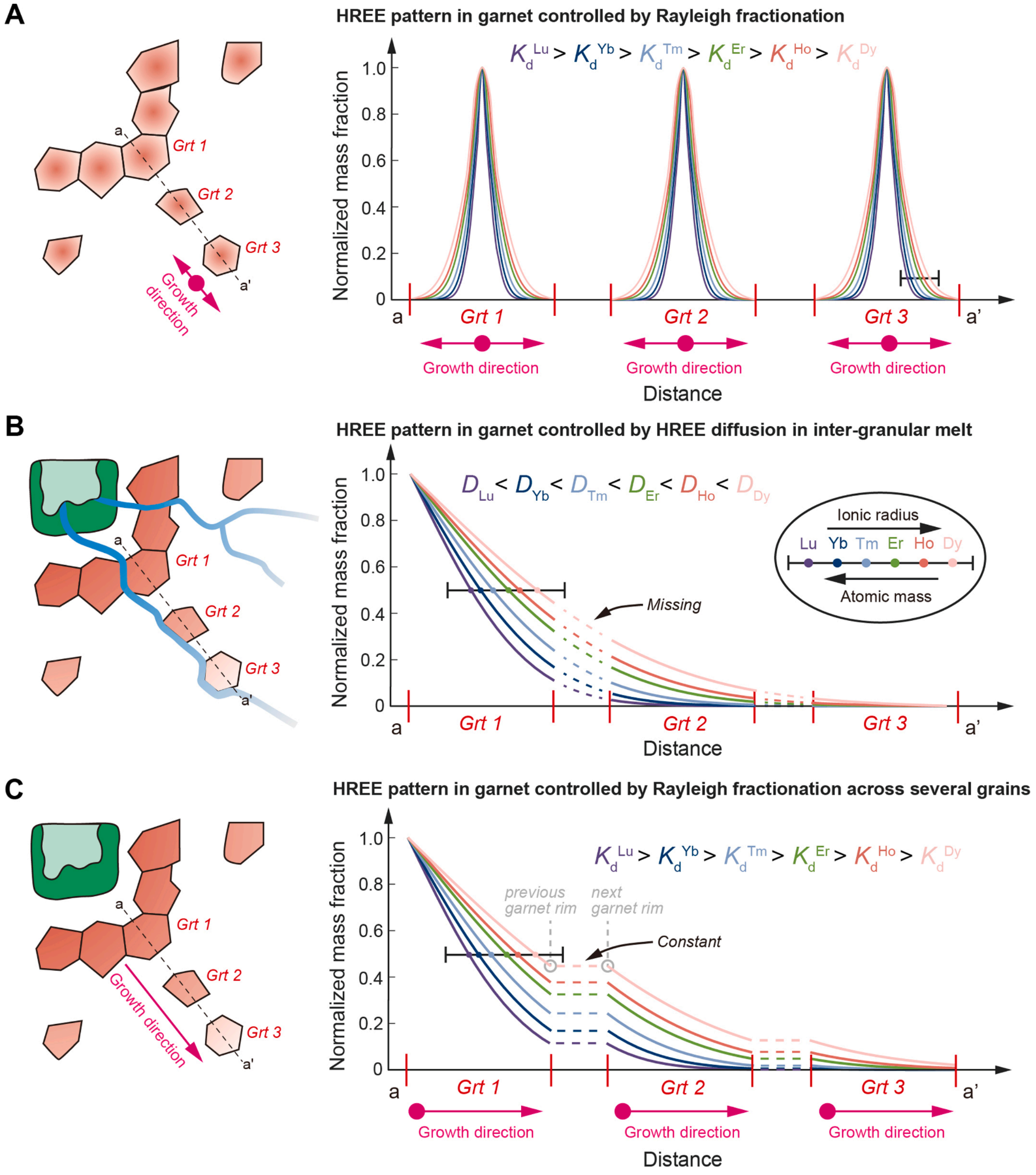

Fig. 11. Cartoon depicting different HREE patterns in garnet formed in different mechanisms. The left figure represents garnet growth in different conditions, while the right figure means the HREE patterns across several garnet grains along the a-a' dashed line. (A) HREE pattern in garnet controlled by Rayleigh fractionation. In each single garnet, HREE decrease from core to the rim, following the K_d of HREE between garnet and bulk rock. K_d of HREE increases with their atom mass. (B) HREE pattern in garnet controlled by HREE diffusion in the inter-granular melt. The HREE gradients represent different diffusivities of HREE in the inter-granular melt, which increases with the decrease of their atom mass. The dotted lines represent "missing" HREE between two garnet grains, as these HREE+Y in melt was not absorbed by available garnet nearby. (C) HREE pattern in garnet controlled by Rayleigh fractionation across several garnet grains. The pink spot and arrow represent the nucleation point and growth direction. The mechanism is similar with A, however the HREE pattern across several garnet grains rather than a single grain. The dotted lines represent constant HREE mass fraction between different garnet grains.

controlled processes, and therefore the rates/timescales of a metamorphic reaction depend on the slower process (Carlson, 1989, 1991, 2011; Daniel and Spear, 1998; Fisher, 1978; Kretz, 1973; Spear and Daniel, 1998; Spear and Daniel, 2001). In our case, the metamorphic reaction is diffusion-controlled because garnet growth (interface-controlled process) must be much faster than HREE+Y diffusion if it is to record the diffusion profile in the melt before the profiles are smoothed. Therefore, the timescale of diffusion in the melt was quantitatively constrained and interpreted to represent the timescale of metamorphic reaction.

Using diffusion modeling with a fixed boundary model, we obtained an optimal diffusion time of 8.4 (+5.4/-3.3) days. The uncertainties propagated from diffusivities and temperature can be considered minimum values as other uncertainty sources like measured data analysis and the goodness of curve fitting were not considered (e.g., Wu et al., 2022). In addition, the effects of porosity and tortuosity on diffusivity are usually considered for a fluid-rock system (e.g., Watson and Baxter, 2007). In our case, HREE+Y diffusion is considered only in the inter-granular melt, and does not occur in the other minerals in the rock. In other words, HREE+Y diffusion is considered in a medium made of 100 % melt, where the effect of porosity is disregarded. However, we have to consider the effect of tortuosity as it reflects the effect of the shape and size of minerals on an actual diffusion path/distance (Oelkers, 1996), and further affects the effective diffusivity and diffusion timescale

(Watson and Baxter, 2007):

$$q = \frac{\text{true path}}{\text{direct path}} \tag{11}$$

$$D_{\text{eff}} = D_{\text{exp}} {}^* q \tag{12}$$

where q is the tortuosity, “true path” means the “melt path” in our case, D_{eff} is the effective diffusivity, D_{exp} is the experimental diffusivity. The porosity is considered as 1 and thus omitted in Eq. (12) (see Watson and Baxter, 2007). We measured the length of possible “melt paths” in 2D and the “direct paths” for the six transects, and estimated the tortuosity according to Eq. (11), which ranges from 0.75 to 0.93 (Fig. S11). This would decrease the effective diffusivity [Eq. (12)] and increase the diffusion timescale by 1.07–1.33 times ($1/q$), resulting in durations of 9 (+5.8/-3.5) or 11.2 (+7.2/-4.4) days. We thus conclude that, in our case, tortuosity insignificantly affects diffusion time.

The effects of interface-controlled process on the diffusion timescale were also partially explored, i.e., the diffusion process accompanying the dissolution of igneous clinopyroxene. As shown in the diffusion modeling results with a moving clinopyroxene boundary, the diffusion profiles become increasingly flat with increasing timescales (Fig. 10B). Visibly significant diffusion gradients are preserved at timescales ranging from a day to a year, and are almost smoothed out at ten years or longer, indicating that the metamorphic reaction occurred within a year. This ultra-fast reaction timescale is comparable to the diffusion modeling with a fixed clinopyroxene boundary. In the moving boundary models, there is a high plateau in the HREE+Y diffusion profile closest to the “current Cpx_I-melt interface”, when diffusion timescales are as short as one day. This indicates that the HREE+Y in this area of melt did not diffuse within this very short timescale. This type of plateau can be observed in the HREE+Y diffusion profiles of transect 1 (Fig. S9G), and the high plateau composition was therefore not considered in the diffusion modeling with fixed boundary model.

5.3. Igneous and metamorphic history of metagabbro B

The petrological and geochronological investigations of metagabbro B distinguished between the magmatic emplacement at ca. 2060 Ma (zircon core U–Pb age, Fig. S5D), from the incomplete metamorphic transformation at ca. 1845 Ma (zircon rim U–Pb age, Fig. S5D) (Fig. 12). The coarse-grained igneous clinopyroxene and plagioclase were consumed in small amounts during prograde metamorphism and formed minor amounts of Grt_LTE. Some amphibole or other metamorphic minerals may also have grown during the prograde stage if fluid was available. Near the peak metamorphic stage at ca. 1845 Ma (Fig. S5D), metagabbro B was metastable at conditions of ~ 800 °C / 0.8 GPa. With the addition of H_2O, the igneous minerals were further consumed, forming the multi-layered corona and ~ 10 vol% rhyolitic melt. The source of H_2O is difficult to constrain, but may have been derived from the metamorphic dehydration of the surrounding TTG and sedimentary country rocks. The presence of H_2O triggered the partial melting reactions, and the melt distributed in the inter-granular medium provided the medium for element diffusion.

During the metamorphic stage, the resorption of igneous clinopyroxene released HREE+Y, which diffused away from the dissolution site in the melt (Fig. 12). The HREE+Y were mostly sequestered by the growth of peritectic Grt_HTE as they are compatible in garnet, and the distribution coefficient $D_{\text{HREE+Y}}$ between garnet and melt is significantly higher (6–20 in Nehring et al., 2009; 38–82 in Taylor et al., 2015) than that between plagioclase or amphibole and melt (<3; Nehring et al., 2009). Diffusion profiles established in the melt were captured by garnet grains during their growth. When the reaction ceased, trace element diffusion profiles were “frozen” within the garnet corona texture and preserved due to the very limited post-growth intra-crystalline diffusion. The “frozen-in” textures and chemical gradients in metagabbro B provide a unique opportunity to quantify the timescale of a metamorphic reaction using diffusion modeling, when a single pulse of mineral growth is dominated by diffusion-controlled processes in the presence of melt during granulite facies metamorphism.

5.4. Is ultra-fast metamorphic reaction unique or common in nature?

In order to compare our results with those of Baxter and DePaolo (2000) and Baxter (2003), who summarized metamorphic reaction rates in experimental and natural systems, we reviewed the timescales of various metamorphic processes. The timescales of natural metamorphic processes operate at different spatial scales (Fig. 13; Table S9). Regional metamorphism spans 100′s of kilometers at tectonic plate margins and

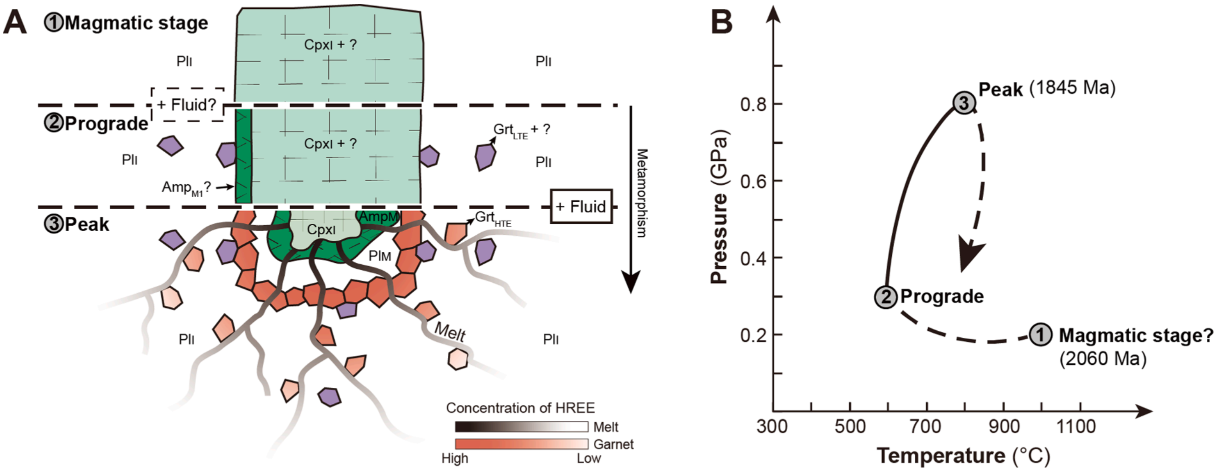

Fig. 12. Magmatic and metamorphic history of metagabbro B. (A) Metamorphic reaction in metagabbro B during regional granulite-facies metamorphism. ① During the magmatic stage (ca. 2060 Ma), mafic magma intruded the TTG and coarse-grained igneous minerals (mainly clinopyroxene and plagioclase) were formed. ② During prograde granulite-facies metamorphism (> ca. 1845 Ma), the igneous clinopyroxene and plagioclase were slightly consumed and formed a small amount of garnet grains (Grt_LTE), metamorphic amphibole and other minerals may also be formed if there was fluid provided. ③ At peak metamorphism (ca. 1845 Ma) when fluid entered the metastable rock, relic igneous minerals were partially dissolved, resulting in the formation of ~10 vol% rhyolitic melt and the multi-layered corona at the boundary between igneous clinopyroxene and plagioclase. During this reaction, the HREE+Y was released by the resorption of igneous clinopyroxene and diffused in the melt away from Cpx_I to the Pl_I. Most of these trace elements were absorbed by the growing garnet grains (Grt_HTE). Therefore, garnet can be used as a proxy to estimate the original diffusion compositional profiles in the melt. (B) Schematic P–T path of metagabbro during magmatic and metamorphic processes.

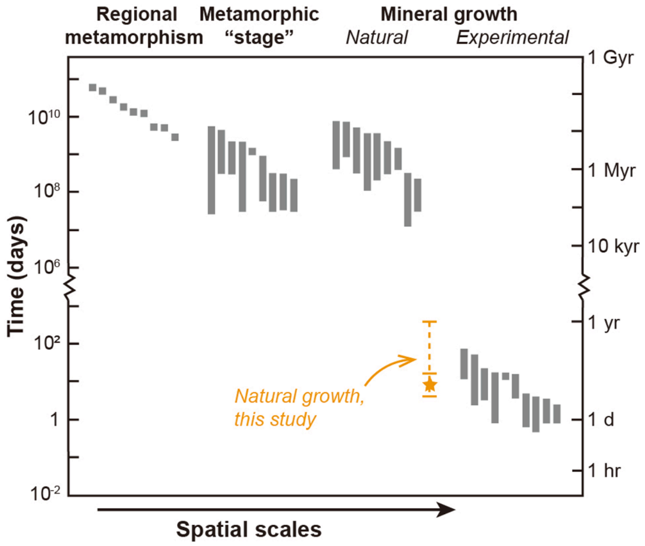

Fig. 13. Timescales of metamorphic processes ranging from regional metamorphism to single mineral growth. Estimated timescales for regional metamorphism, a single metamorphic "stage", and mineral growth. Grey boxes represent estimates of timescales (ranges) from individual studies; references list is provided in Table S9 and supplementary material. The orange star with the error bar shows the growth duration with uncertainty obtained in this study, 8.4 (+5.4/-3.3) days (diffusion modeling with fixed boundary model) and one year (diffusion modeling with moving boundary model). Abbreviations: hr-hours, d-days, yr-years, kyr-thousands of years, Myr-million years, Gyr-billion years.

lasts 8–200 Myrs, with shorter transformation stages of 0.1–10 Myrs preserved in the rock record. Studies of the growth of a single metamorphic mineral in natural rocks suggest timescales of 0.1–17 Myrs. These estimated natural timescales are 5–11 orders of magnitude longer than those observed in experimental studies, where minerals grow within hours to months. Baxter and DePaolo (2000) and Baxter (2003) discuss this discrepancy, suggesting that metamorphic reactions in nature may be rate-limited by factors like grain size, driving force for the reaction, rates of inter-granular transport and fluid content. They highlight the fluid content as the key factor, resulting in the different rates between natural regional metamorphism (less free fluid) vs. natural contact metamorphism and lab metamorphism (generally fluid saturated).

Our diffusion modeling results from metagabbro B are consistent with the timescales of metamorphic reactions in the lab-based experiments; and its reaction rate of 0.288 g/cm^2/year [following the calculation method in Baxter (2003)] is consistent with the reaction rates of lab data and contact metamorphism with more free fluid (Baxter, 2003). At least in this case, there is no need for an additional rate-limiting process to explain the variable metamorphic reaction rates (or growth rates) found between natural and experimental systems. One reason for the inconsistency of mineral growth timescales between natural and experimental systems (Fig. 13) may be the insufficient temporal resolution of radioisotope dating methods to resolve stages of ultra-fast mineral growth. In addition, metamorphic reaction rates in natural systems may not be as constant and continuous as in experimental systems; instead, they might be pulse-growth depending on the evolving temperature, pressure, and particularly fluid of the environment (e.g., Ague and Baxter, 2007; Baxter, 2003; Cruz-Uribe et al., 2014; Dragovic et al., 2015; Pattison et al., 2011; Rubie, 1986; Thompson, 1983; Tual et al., 2022). Our study shows that a single pulse of mineral growth in a natural sample can occur within a year if in the presence of melt, which is consistent with experimental results (Fig. 13). It is also possible that previous results for metamorphic systems may represent average timescales for mineral growth, including relatively fast growth pulses and intermittent periods of unreactivity in between. Similarly, some previously estimated reaction rates are time-averaged, assuming constant reaction rates (Baxter, 2003; Cruz-Uribe et al., 2014). In addition, the degree of disequilibrium of the reactants can also affect the dissolution and associated growth rates (Hartmeier et al. 2024).

Our study supports the interpretation that basement rocks at deep crustal levels are dry and likely metastable for significant periods, and that transient fluid infiltration can trigger metamorphic reactions and mineral transformation over short periods (Rubie, 1986, 1998). In addition, water can also catalyze reactions via other mechanisms such as reducing activation energy and creating new diffusion pathways (Rubie, 1986, 1998). Fluid may also increase reactivity in metamorphic rocks via melting reactions. Experimental studies have demonstrated that trace element diffusion in melt increases with water content in the melt (Behrens and Hahn, 2009; Holycross and Watson, 2018; Koepke and Behrens, 2001). Therefore, both fluid and melt have similar properties to catalyze reactions. Unfortunately, evidence of fast mineral growth in the natural record is commonly lost as rocks continue undergoing subsequent metamorphic transformations, recrystallization and deformation, or as primary diffusion profiles are smoothed by intragranular diffusion. We propose that single pulses of metamorphic mineral growth involving fluid/melt in nature could often occur fast, as is known in igneous systems, and in laboratory metamorphic experiments, and fluid-saturated contact metamorphic systems (e.g., Antonelli et al., 2019; Baxter, 2003; Tao et al., 2018). If metamorphic reactions (fluid/melt catalyzed) are instantaneous at geological timescales, changes associated with metamorphism, such as rock volume, density, and strength, as well as melt generation and fluid release could also be instantaneous. How the crust accommodates these rapid changes has implications for our understanding of the physical processes (e.g., rock buoyancy, seismicity, and fluid transport) in the solid Earth.

6. Conclusions

Petrography, bulk-rock geochemistry, metamorphic *P–T* conditions, and geochronology of two metagabbro samples collected thirty meters apart show that they record the same granulite-facies regional metamorphism during the late Paleoproterozoic. At the peak stage, metagabbro A shows the equilibrated granulite-facies assemblage; while metagabbro B partially equilibrated, preserving metastable igneous phases and developing multi-layered metamorphic corona textures. Water budget calculations suggest that different degrees of fluid infiltration during metamorphism may control the formation of different metamorphic reaction textures in the two metagabbros. Multi-phase trace element mapping performed in metagabbro B reveals frozen-in chemical gradients of trace elements (HREE+Y) across a garnet corona texture. Data interpretations, including mass balance calculations, demonstrate that the HREE+Y chemical gradients represent diffusion profiles in the inter-granular melt, which were inherited by different individual garnet grains during their growth. Diffusion modeling with a fixed and moving boundary constrains a single pulse of peritectic garnet growth from a melt to 8.4 (+5.4/-3.3) days, or one year, respectively. These timescales are consistent with those of mineral growth from laboratory-based observations. We suggest that such ultra-fast single pulse of mineral growth/metamorphic reaction could be common in the presence of a transient fluid/melt phase.

CRediT authorship contribution statement

Jia-Hui Liu: Writing – original draft, Validation, Software, Investigation, Funding acquisition, Formal analysis, Conceptualization. **Pierre Lanari:** Writing – original draft, Validation, Supervision, Software, Investigation, Funding acquisition, Formal analysis, Conceptualization, Methodology. **Renée Tamblyn:** Writing – review & editing, Validation, Formal analysis, Conceptualization, Investigation. **Hugo Dominguez:** Validation, Software, Methodology, Writing – Review & Editing. **Jörg**

Hermann: Writing – review & editing, Validation, Conceptualization. **Daniela Rubatto:** Writing – review & editing, Validation, Conceptualization. **Jacob B. Forshaw:** Writing – review & editing, Validation, Conceptualization. **Francesca Piccoli:** Resources, Investigation, Writing – Review & Editing. **Qian W.L. Zhang:** Writing – review & editing, Validation, Investigation, Funding acquisition. **Thorsten A. Markmann:** Investigation, Writing – Review & Editing. **Julien Reynes:** Investigation, Writing – Review & Editing. **Zhen M.G. Li:** Investigation, Writing – Review & Editing. **Shujuan Jiao:** Writing – review & editing, Validation. **Jinghui Guo:** Writing – review & editing, Validation, Supervision, Funding acquisition.

Data availability

The source code for diffusion modeling is available through Github at https://github.com/LIU-Jiahui/REE_diffusion_Liu2024. The complete chemical datasets are available through Zenodo at https://doi.org/10.5281/zenodo.7924560.

Declaration of competing interest

The authors declare that they have no known competing financial interests or personal relationships that could have appeared to influence the work reported in this paper.

Acknowledgments

Ethan Baxter, Ralf Halama, and one anonymous reviewer are thanked for their constructive and detailed comments and suggestions, which have significantly improved the manuscript. Olivier Namur, Jeffrey Catalano and Hailiang Dong are thanked for their efficient editorial handling. We thank Juan Wang, Jiao Li, and Xiao-Xiao Ling for their assistance during experimental investigations. The first author appreciates discussions with Prof. Matthew Kohn and Prof. Yi Chen. This study was funded by the European Research Council (ERC) under the European Union's Horizon 2020 research and innovation program (850530), the National Natural Science Foundation of China (42330304, 42302220), the China National Postdoctoral Program for Innovative Talents (BX20220294), and the Fundamental Research Funds for the Central Universities (E2E40401X2).

Appendix A. Supplementary material

Supplementary materials include supplementary methods, results, figures and tables. A total of eleven figures and nine tables are provided as supplementary materials, including measured results of geochemistry data, geochronological data, and mineral water content data, modeled results of phase equilibrium modeling and diffusion modeling, calculation results of water budget and mass balance of HREE+Y in igneous and metamorphic stages, and a database of the timescales of metamorphic processes. Supplementary material to this article can be found online at https://doi.org/10.1016/j.gca.2025.01.036.

References

Ague, J.J., Baxter, E.F., 2007. Brief thermal pulses during mountain building recorded by Sr diffusion in apatite and multicomponent diffusion in garnet. *Earth and Planetary Science Letters* 261, 500–516.

Antonelli, M.A., Mittal, T., McCarthy, A., Tripoli, B., Watkins, J.M., DePaolo, D.J., 2019. Ca isotopes record rapid crystal growth in volcanic and subvolcanic systems. *Proc Natl Acad Sci U S A* 116, 20315–20321.

Ashworth, J., Sheplev, V., 1997. Diffusion modelling of metamorphic layered coronas with stability criterion and consideration of affinity. *Geochimica et Cosmochimica Acta* 61, 3671–3689.

Bank, R. E., Coughran, W. M., Fichtner, W., Grosse, E. H., Rose and D. J. (1985) Transient Simulation of Silicon Devices and Circuits. *Computer-Aided Design of Integrated Circuits and Systems, IEEE Transactions on*.

Baxter, E.F., 2003. Natural constraints on metamorphic reaction rates. *Geological Society, London, Special Publications* 220, 183–202.

Baxter, E.F., DePaolo, D.J., 2000. Field measurement of slow metamorphic reaction rates at temperatures of 500 to 600 C. *Science* 288, 1411–1414.

Behrens, H., Hahn, M., 2009. Trace element diffusion and viscous flow in potassium-rich trachytic and phonolitic melts. *Chemical Geology* 259, 63–77.

Bezanson, J., Edelman, A., Karpinski, S., Shah, V.B., 2017. Julia: A Fresh Approach to Numerical Computing. SIAM Review 59, 65–98.

Bloch, E., Jollands, M., Devoir, A., Bouvier, A.-S., Ibañez-Mejia, M., Baumgartner, L., 2020. Multispecies diffusion of yttrium, rare earth elements and hafnium in garnet. *Journal of Petrology* 61, egaa055.

Camacho, A., Lee, J.K., Hensen, B.J., Braun, J., 2005. Short-lived orogenic cycles and the eclogitization of cold crust by spasmodic hot fluids. *Nature* 435, 1191–1196.

Caracciolo, A., Kahl, M., Bali, E., Guðfinnsson, G.H., Halldórsson, S.A., Hartley, M.E., 2021. Timescales of crystal mush mobilization in the Bárðarbunga-Veiðivötn volcanic system based on olivine diffusion chronometry. *American Mineralogist* 106, 1083–1096.

Carlson, W., 1989. The significance of intergranular diffusion to the mechanisms and kinetics of porphyroblast crystallization. *Beiträage Zur Mineralogie Und Petrographie* 103, 1–24.

Carlson, W., 1991. Competitive Diffusion-Controlled Growth of Porphyroblasts. *Mineralogical Magazine - MINER MAG* 55, 317–330.

Carlson, W.D., 2006. Rates of Fe, Mg, Mn, and Ca diffusion in garnet. *American Mineralogist* 91, 1–11.

Carlson, W.D., 2010. Dependence of reaction kinetics on H_2O activity as inferred from rates of intergranular diffusion of aluminium. *Journal of Metamorphic Geology* 28, 735–752.

Carlson, W.D., 2011. Porphyroblast crystallization: linking processes, kinetics, and microstructures. *International Geology Review* 53, 406–445.

Carlson, W.D., 2012. Rates and mechanism of Y, REE, and Cr diffusion in garnet. *American Mineralogist* 97, 1598–1618.

Chakraborty, S., Anczkiewicz, R., Gaidies, F., Rubatto, D., Sorcar, N., Faak, K., Mukhopadhyay, D., Dasgupta, S., 2016. A review of thermal history and timescales of tectonometamorphic processes in Sikkim Himalaya (NE India) and implications for rates of metamorphic processes. *Journal of Metamorphic Geology* 34, 785–803.

Chu, X., Ague, J.J., Podladchikov, Y.Y., Tian, M., 2017. Ultrafast eclogite formation via melting-induced overpressure. *Earth and Planetary Science Letters* 479, 1–17.

Chu, X., Ague, J.J., Tian, M., Baxter, E.F., Rumble III, D., Chamberlain, C.P., 2018. Testing for Rapid Thermal Pulses in the Crust by Modeling Garnet Growth–Diffusion–Resorption Profiles in a UHT Metamorphic 'Hot Spot', New Hampshire, USA. Journal of Petrology 59, 1939–1964.

Cicconi, M.R., Giuli, G., Paris, E., Courtial, P., Dingwell, D., 2013. XAS investigation of rare earth elements in sodium disilicate glasses. *Journal of Non-Crystalline Solids* 362, 162–168.

Connolly, J.A.D., 2005. Computation of phase equilibria by linear programming: A tool for geodynamic modeling and its application to subduction zone decarbonation (Article). *Earth and Planetary Science Letters* 236, 524–541.

Costa, F., Chakraborty, S., Dohmen, R., 2003. Diffusion coupling between trace and major elements and a model for calculation of magma residence times using plagioclase. *Geochimica et Cosmochimica Acta* 67, 2189–2200.

Crank, J., 1975. The mathematics of diffusion. Clarendon Press, Oxford.

Cruz-Uribe, A.M., Feineman, M.D., Zack, T., Barth, M., 2014. Metamorphic reaction rates at~ 650–800° C from diffusion of niobium in rutile. *Geochimica et Cosmochimica Acta* 130, 63–77.

Daniel C. and Spear F. (1998) 3-Dimensional patterns of garnet nucleation and growth. *Geology* **26**.

Dragovic, B., Baxter, E.F., Caddick, M.J., 2015. Pulsed dehydration and garnet growth during subduction revealed by zoned garnet geochronology and thermodynamic modeling, Sifnos, Greece. *Earth and Planetary Science Letters* 413, 111–122.

Du, K.-Y., Cheng, H., Dragovic, B., Cao, C., 2023. Dating corona formation in high-grade rocks: integrated garnet and zircon petrochronology of granulite-facies rocks in the North China Craton. *Contributions to Mineralogy and Petrology* **178**.

Fisher, G., 1978. Rate laws in metamorphism. *Geochimica et Cosmochimica Acta* 42 (1035–1041), 1043–1050.

Gaidies, F., Milke, R., Heinrich, W., Abart, R., 2017. Metamorphic mineral reactions: Porphyroblast, corona and symplectite growth. Microstructures, textures, chemical and isotopic signatures, In Mineral reaction kinetics, pp. 469–540.

Ghosh, S., Prabhakar, N., D'Souza, J., 2021. Origin of multilayer corona textures in mafic granulites from the Sandmata Complex, Aravalli Craton (northwestern India): petrological characteristics and tectonic implications. *Contributions to Mineralogy and Petrology* **176**.

Glicksman M. E. (2011) Principles of solidification: An introduction to modern casting and crystal growth concepts.

Grant, S.M., 1988. Diffusion models for corona formation in metagabbros from the Western Grenville Province, Canada. *Contributions to Mineralogy and Petrology* 98, 49–63.

Green, E.C.R., White, R.W., Diener, J.F.A., Powell, R., Holland, T.J.B., Palin, R.M., 2016. Activity-composition relations for the calculation of partial melting equilibria in metabasic rocks. *Journal of Metamorphic Geology* 34, 845–869.

Hartmeier, P., Lanari, P., Forshaw, J.B., Markmann, T.A., 2024. Tracking Garnet Dissolution Kinetics in 3D Using Deep Learning Grain Shape Classification. *Journal of Petrology* 65, 1–9.

Hellstrom, J., Paton, C., Woodhead, J., Hergt, J., 2008. Iolite: software for spatially resolved LA-(quad and MC) ICPMS analysis. *Mineralogical Association of Canada Short Course Series* 40, 343–348.

Holland, T., Powell, R., 2003. Activity–composition relations for phases in petrological calculations: an asymmetric multicomponent formulation. *Contributions to Mineralogy and Petrology* 145, 492–501.

Holland, T.J.B., Powell, R., 2011. An improved and extended internally consistent thermodynamic dataset for phases of petrological interest, involving a new equation of state for solids. *Journal of Metamorphic Geology* 29, 333–383.

Hollister, L.S., 1966. Garnet zoning - An interpretation based on rayleigh fractionation model. *SCIENCE* 154, 1647.

Holycross, M.E., Watson, B.E., 2016. Diffusive fractionation of trace elements in basaltic melt. *Contributions to Mineralogy and Petrology* 171, 80.

Holycross, M.E., Watson, E.B., 2018. Trace element diffusion and kinetic fractionation in wet rhyolitic melt. *Geochimica et Cosmochimica Acta* 232, 14–29.

Incel, S., Hilairet, N., Labrousse, L., John, T., Deldicque, D., Ferrand, T., Wang, Y., Renner, J., Morales, L., Schubnel, A., 2017. Laboratory earthquakes triggered during eclogitization of lawsonite-bearing blueschist. *Earth and Planetary Science Letters* 459, 320–331.

Jochum, K.P., Willbold, M., Raczek, I., Stoll, B., Herwig, K., 2005. Chemical Characterisation of the USGS Reference Glasses GSA-1G, GSC-1G, GSD-1G, GSE-1G, BCR-2G, BHVO-2G and BIR-1G Using EPMA, ID-TIMS, ID-ICP-MS and LA-ICP-MS. *Geostandards and Geoanalytical Research* 29, 285–302.

Joesten, R., 1977. Evolution of mineral assemblage zoning in diffusion metasomatism. *Geochimica et Cosmochimica Acta* 41, 649–670.

Johnson, C., Carlson, W., 1990. The origin of olivine-plagioclase coronas in metagabbros from the Adirondack Mountains, New York. *Journal of Metamorphic Geology* 8, 697–717.

Jollands, M.C., Hanger, B.J., Yaxley, G.M., Hermann, J., Kilburn, M.R., 2018. Timescales between mantle metasomatism and kimberlite ascent indicated by diffusion profiles in garnet crystals from peridotite xenoliths. *Earth and Planetary Science Letters* 481, 143–153.

King, D.S., Zimmerman, M.E., Kohlstedt, D.L., 2010. Stress-driven melt segregation in partially molten olivine-rich rocks deformed in torsion. *Journal of Petrology* 51, 21–42.

Koepke, J., Behrens, H., 2001. Trace element diffusion in andesitic melts: An application of synchrotron X-ray fluorescence analysis. *Geochimica et Cosmochimica Acta* 65, 1481–1498.

Kohn, M.J., Spear, F.S., 2000. Retrograde net transfer reaction insurance for pressure-temperature estimates. *Geology* 28, 1127–1130.

Kretz, R., 1973. Kinetics of the crystallization of garnet at two localities near Yellowknife. *The Canadian Mineralogist* 12.

Lanari, P., Engi, M., 2017. Local bulk composition effects on metamorphic mineral assemblages. *Reviews in Mineralogy and Geochemistry* 83, 55–102.

Lanari P., Laughton J., Tedeschi M. and Markmann T. (2023) XMapTools 4.1 (v4.1). *Zenodo* https://doi.org/10.5281/zenodo.7656958.

Lanari, P., Piccoli, F., 2020. New horizons in quantitative compositional mapping – Analytical conditions and data reduction using XMapTools. *IOP Conference Series: Materials Science and Engineering* 891, 012016.

Lanari, P., Vidal, O., De Andrade, V., Dubacq, B., Lewin, E., Grosch, E.G., Schwartz, S., 2014. XMapTools: A MATLAB©-based program for electron microprobe X-ray image processing and geothermobarometry. *Computers & Geosciences* 62, 227–240.

Lanari, P., Vho, A., Bovay, T., Airaghi, L., Centrella, S., 2019. Quantitative compositional mapping of mineral phases by electron probe micro-analyser. *Geological Society, London, Special Publications* 478, 39–63.

Larikova, T.L., Zaraisky, G.P., 2009. Experimental modelling of corona textures. *Journal of Metamorphic Geology* 27, 139–151.

Liu, J.-H., Zhang, Q.W.L., Wang, J., Zhang, H.C.G., Wu, C.-M., 2021. Metamorphic evolution and SIMS U–Pb geochronology of orthopyroxene-bearing high-P semipelitic granulite in the Fuping area, middle Trans-North China Orogen. *Journal of Metamorphic Geology* 39, 297–320.

Malvoisin, B., Austrheim, H., Hetényi, G., Reynes, J., Hermann, J., Baumgartner, L.P., Podladchikov, Y.Y., 2020. Sustainable densification of the deep crust. Geology 48, 673–677.

Markmann, T.A., Lanari, P., Piccoli, F., Pettke, T., Tamblyn, R., Tedeschi, M., Lueder, M., Kunz, B.E., Riel, N., Laughton, J., 2024. Multi-phase quantitative compositional mapping by LA-ICP-MS: Analytical approach and data reduction protocol implemented in XMapTools. Chem. Geol. 646, 121895.

Meek, U., Piazolo, S., Daczko, N., 2019. The field and microstructural signatures of deformation-assisted melt transfer: Insights from magmatic arc lower crust, New Zealand. *Journal of Metamorphic Geology* 37.

Miyashiro, A., Shido, F., 1980. Differentiation of gabbros in the Mid-Atlantic Ridge near 24 N. *Geochemical Journal* 14, 145–154.

Molina, J., Poli, S., 1998. Singular equilibria in paragonite blueschists, amphibolites and eclogites. *Journal of Petrology* 39, 1325–1346.

Müller, T., Dohmen, R., Becker, H., Ter Heege, J.H., Chakraborty, S., 2013. Fe–Mg interdiffusion rates in clinopyroxene: experimental data and implications for Fe–Mg exchange geothermometers. *Contributions to Mineralogy and Petrology* 166, 1563–1576.

Nehring, F., Foley, S.F., Hölttä, P., 2009. Trace element partitioning in the granulite facies. *Contributions to Mineralogy and Petrology* 159, 493–519.

Neogi, S., Bolton, E.W., Chakraborty, S., 2014. Timescales of disequilibrium melting in the crust: constraints from modelling the distribution of multiple trace elements and a case study from the Lesser Himalayan rocks of Sikkim. *Contributions to Mineralogy and Petrology* 168, 1–22.

Obara, K., 2002. Nonvolcanic deep tremor associated with subduction in southwest Japan. *Science* 296, 1679–1681.

Oelkers, E.H., 1996. Physical and chemical properties of rocks and fluids for chemical mass transport calculations. *Reviews in Mineralogy* 34, 131–192.

Ogilvie, P., Gibson, R.L., 2017. Arrested development – a comparative analysis of multilayer corona textures in high-grade metamorphic rocks. *Solid Earth* 8, 93–135.

Otamendi, J.E., de la Rosa, J.D., Douce, A.E.P., Castro, A., 2002. Rayleigh fractionation of heavy rare earths and yttrium during metamorphic garnet growth. *Geology* 30, 159–162.

Paton, C., Hellstrom, J., Paul, B., Woodhead, J., Hergt, J., 2011. Iolite: Freeware for the visualisation and processing of mass spectrometric data. *Journal of Analytical Atomic Spectrometry* 26, 2508–2518.

Pattison, D.R.M., De Capitani, C., Gaidies, F., 2011. Petrological consequences of variations in metamorphic reaction affinity. *Journal of Metamorphic Geology* 29, 953–977.

Pearce, N.J., Perkins, W.T., Westgate, J.A., Gorton, M.P., Jackson, S.E., Neal, C.R., Chenery, S.P., 1997. A compilation of new and published major and trace element data for NIST SRM 610 and NIST SRM 612 glass reference materials. *Geostandards Newsletter* 21, 115–144.

Phelps, P.R., Lee, C.-T.-A., Morton, D.M., 2020. Episodes of fast crystal growth in pegmatites. *Nature Communications* 11, 1–10.

Pitcairn, I.K., Leventis, N., Beaudoin, G., Faure, S., Guilmette, C., Dubé, B., 2021. A metasedimentary source of gold in Archean orogenic gold deposits. *Geology* 49, 862–866.

Pollington, A.D., Baxter, E.F., 2010. High resolution Sm–Nd garnet geochronology reveals the uneven pace of tectonometamorphic processes. *Earth and Planetary Science Letters* 293, 63–71.

Powell, R., Holland, T.J.B., 2008. On thermobarometry. *Journal of Metamorphic Geology* 26, 155–179.

Rackauckas, C., Nie, Q., 2017. DifferentialEquations.jl – A Performant and Feature-Rich Ecosystem for Solving Differential Equations in Julia. *Journal of Open Research Software* 5.

Revels J., Lubin M. and Papamarkou T. (2016) Forward-Mode Automatic Differentiation in Julia.

Ross K. and Elthon D. Cumulus and postcumulus crystallization in the oceanic crust: major-and trace-element geochemistry of Leg 153 gabbroic rocks. *Proceedings-Ocean Drilling Program Scientific Results*. National Science Foundation.

Rubatto, D., Burger, M., Lanari, P., Hattendorf, B., Schwarz, G., Neff, C., Schmidt, P.K., Hermann, J., Vho, A., Günther, D., 2020. Identification of growth mechanisms in metamorphic garnet by high-resolution trace element mapping with LA-ICP-TOFMS. *Contributions to Mineralogy and Petrology* 175, 1–19.

Rubie, D.C., 1986. The catalysis of mineral reactions by water and restrictions on the presence of aqueous fluid during metamorphism. *Mineralogical Magazine* 50, 399–415.

Rubie, D.C., 1998. Disequilibrium during metamorphism: the role of nucleation kinetics. *Geological Society, London, Special Publications* 138, 199–214.

Rubie, D., Thompson, A., 1985. Kinetics of metamorphic reactions at elevated temperatures and pressures: an appraisal of available experimental data. In: *Metamorphic Reactions: Kinetics, Textures, and Deformation*. Springer, pp. 27–79.

Spear, F., Daniel, C., 1998. Three-dimensional imaging of garnet porphyroblast sizes and chemical zoning: Nucleation and growth history in the garnet zone. *Geological Materials Research* 1.

Spear, F.S., Daniel, C.G., 2001. Diffusion control of garnet growth, Harpswell Neck, Maine, USA. *Journal of Metamorphic Geology* 19, 179–195.

Spear, F.S., Kohn, M.J., Florence, F.P., Menard, T., 1990. A model for garnet and plagioclase growth in pelitic schists: implications for thermobarometry and P-T path determinations. *Journal of Metamorphic Geology* 8, 683–696.

Tao, R., Fei, Y., Bullock, E.S., Xu, C., Zhang, L., 2018. Experimental investigation of Fe^{3+}-rich majoritic garnet and its effect on majorite geobarometer. *Geochimica et Cosmochimica Acta* 225, 1–16.

Taylor, R.J.M., Harley, S.L., Hinton, R.W., Elphick, S., Clark, C., Kelly, N.M., 2015. Experimental determination of REE partition coefficients between zircon, garnet and melt: a key to understanding high-T crustal processes. *Journal of Metamorphic Geology* 33, 231–248.

Thompson, A.B., 1983. Fluid-absent metamorphism. *Journal of the Geological Society* 140, 533–547.

Tirone, M., Ganguly, J., Dohmen, R., Langenhorst, F., Hervig, R., Becker, H.-W., 2005. Rare earth diffusion kinetics in garnet: Experimental studies and applications. *Geochimica et Cosmochimica Acta* 69, 2385–2398.

Tual, L., Smit, M.A., Cutts, J., Kooijman, E., Kielman-Schmitt, M., Majka, J., Foulds, I., 2022. Rapid, paced metamorphism of blueschists (Syros, Greece) from laser-based zoned Lu-Hf garnet chronology and LA-ICPMS trace element mapping. *Chemical Geology* 607, 121003.

Van Orman, J.A., Grove, T.L., Shimizu, N., Layne, G.D., 2002. Rare earth element diffusion in a natural pyrope single crystal at 2.8 GPa. *Contributions to Mineralogy and Petrology* 142, 416–424.

Viete, D.R., Lister, G.S., 2017. On the significance of short-duration regional metamorphism. *Journal of the Geological Society* 174, 377–392.

Walther, J.V., Wood, B.J., 1984. Rate and mechanism in prograde metamorphism. *Contributions to Mineralogy and Petrology* 88, 246–259.

Wang, K., Cassidy, J.F., Wada, I., Smith, A.J., 2004. Effects of metamorphic crustal densification on earthquake size in warm slabs. *Geophysical Research Letters* 31, L01605.

Warr, L.N., 2021. IMA–CNMNC approved mineral symbols. *Mineralogical Magazine* 85, 291–320.

Watson, E.B., Baxter, E.F., 2007. Diffusion in solid-Earth systems. *Earth and Planetary Science Letters* 253, 307–327.

Watson, E.B., Müller, T., 2009. Non-equilibrium isotopic and elemental fractionation during diffusion-controlled crystal growth under static and dynamic conditions. *Chemical Geology* 267, 111–124.

White, R.W., Powell, R., Holland, T.J.B., Worley, B.A., 2000. The effect of TiO_2 and Fe_2O_3 on metapelitic assemblages at greenschist and amphibolite facies conditions:

mineral equilibria calculations in the system K_2O–FeO–MgO–Al_2O_3–SiO_2–H_2O–TiO_2–Fe_2O_3. *Journal of Metamorphic Geology* 18, 497–511.

White, R.W., Powell, R., Clarke, G.L., 2002. The interpretation of reaction textures in Fe-rich metapelitic granulites of the Musgrave Block, central Australia: constraints from mineral equilibria calculations in the system K_2O-FeO-MgO-Al_2O_3-SiO_2-H_2O-TiO_2-Fe_2O_3. *Journal of Metamorphic Geology* 20, 41–55.

White, R.W., Powell, R., Baldwin, J.A., 2008. Calculated phase equilibria involving chemical potentials to investigate the textural evolution of metamorphic rocks. *Journal of Metamorphic Geology* 26, 181–198.

White, R.W., Powell, R., Johnson, T.E., 2014a. The effect of Mn on mineral stability in metapelites revisited: new a–x relations for manganese-bearing minerals. *Journal of Metamorphic Geology* 32, 809–828.

White, R.W., Powell, R., Holland, T.J.B., Johnson, T.E., Green, E.C.R., 2014b. New mineral activity-composition relations for thermodynamic calculations in metapelitic systems. *Journal of Metamorphic Geology* 32, 261–286.

Wu, L.-G., Li, Y., Jollands, M.C., Vermeesch, P., Li, X.-H., 2022. Diffuser: A user-friendly program for diffusion chronometry with robust uncertainty estimation. *Computers & Geosciences* 163, 105108.

Zhao, G.C., Wilde, S.A., Cawood, P.A., Lu, L.Z., 2000. Petrology and P-T path of the Fuping mafic granulites: implications for tectonic evolution of the central zone of the North China craton. *Journal of Metamorphic Geology* 18, 375–391.

Zhao, G.C., Sun, M., Wilde, S.A., Li, S.Z., 2005. Late Archean to Paleoproterozoic evolution of the North China Craton: key issues revisited. *Precambrian Research* 136, 177–202.